

**HANOI UNIVERSITY OF SCIENCE AND TECHNOLOGY  
SCHOOL OF ELECTRICAL AND ELECTRONIC ENGINEERING**



**BACHELOR THESIS**

**RADIAL BASIS FUNCTION BASED INPUT SHAPING  
FOR GANTRY CRANE CONTROL**

**ĐÀO DUY HIẾU**

hieu.dd192202@sis.hust.edu.vn

**Advanced Program of Control and Automation**

**Instructor:** Dr. Đỗ Trọng Hiếu

Instructor's Signature

**Department:** Dept. of Automation

**School:** Electrical and Electronic Engineering

Hanoi, 08/2023



## **BACHELOR THESIS TOPIC**

Full name of student: Đào Duy Hiếu                          Student ID: 20192202

Cohort: 64                          School: School of Electrical and Electronic Engineering

Department: Department of Automation

### **1. Topic**

**Radial Basis Function based Input Shaping for Gantry Crane control**

### **2. Content**

- Investigate the structure and vibration control issues for real-world gantry crane systems.
- Explore the mathematical and experimental models for a single-pendulum gantry crane system with load hoisting process.
- Study and design a control scheme using a combination of Active Disturbance Rejection Controls and Radial Basis Function network-based Input Shaping to control the trolley position, cable length, and mitigate vibrations in the system.
- Conduct effectiveness testing of the proposed control scheme through simulations and its application on the experimental gantry crane system.

3. Topic assignment date: 04, 2023

4. Topic complete date: 08, 2023

August 08th, 2023

**INSTRUCTOR**

## **GRATITUDE**

To successfully complete this project, I would like to sincerely express my gratitude for the dedicated guidance and support from Dr. Đỗ Trọng Hiếu throughout this entire semester. Additionally, I would like to extend my heartfelt thanks to all the members of the WSR research group who wholeheartedly assisted and encouraged me, enabling me to bring this project to fruition. Due to my limited expertise and lack of experience, the content of this project may still require some improvements and revisions. I earnestly hope to receive valuable feedback and guidance from esteemed professors to further enhance this work.

## **ABSTRACT**

Crane systems play a vital role across various industries, offering efficient and dependable solutions for material handling and heavy-load operations. To optimize the system's performance, in this project, two separate Active Disturbance Rejection Control (ADRC) are employed to accurately regulate the movement of the trolley and payload, as well as effectively counteract internal disturbances caused by payload vibration. Additionally, a Radial Basis Function network-based Input Shaping (RBFN-IS) is utilized to minimize payload oscillations during operation. Two networks continuously update the parameters of the Input Shaping (IS) in real-time based on variations in system's parameters. Furthermore, the Particle Swarm Optimization (PSO) algorithm is employed to search for optimal parameters of the IS for specific cable lengths and payload mass, thereby improving vibration suppression capability. The obtained results have successfully validated the utilized method.

Hanoi, August 08th, 2023

Student

**Đào Duy Hiếu**



## TABLE OF CONTENTS

<b>LIST OF ABBREVIATIONS</b>	<b>i</b>
<b>LIST OF FIGURES</b>	<b>iii</b>
<b>LIST OF TABLES</b>	<b>iv</b>
<b>CHAPTER 1. INTRODUCTION</b>	<b>1</b>
1.1 Overview of the crane system . . . . .	1
1.1.1 The structure of the crane system . . . . .	2
1.1.2 Applications of overhead crane . . . . .	4
1.2 Operation problems . . . . .	4
1.3 Chapter's conclusion . . . . .	5
<b>CHAPTER 2: MATHEMATICAL MODEL OF CRANE SYSTEM</b>	<b>6</b>
2.1 Modeling the crane system . . . . .	6
2.2 Verifying the mathematical model . . . . .	8
2.3 Chapter's conclusion . . . . .	14
<b>CHAPTER 3: ACTIVE DISTURBANCE REJECTION CONTROL</b>	<b>15</b>
3.1 Control structure . . . . .	15
3.2 Concept of ADRC . . . . .	16
3.3 Chapter's Conclusion . . . . .	18
<b>CHAPTER 4: RADIAL BASIS FUNCTION-BASED INPUT SHAPING</b>	<b>19</b>
4.1 Concept of Input Shaping . . . . .	19
4.2 Radial Basis Function Network . . . . .	21
4.3 Particle Swarm Optimization . . . . .	23
4.4 Chapter's Conclusion . . . . .	26
<b>CHAPTER 5: RESULTS WITH THE MATHEMATICAL MODEL</b>	<b>27</b>

5.1	Implementation of the control scheme for mathematical model . . . . .	27
5.1.1	Designing the ADRCs . . . . .	27
5.1.2	Designing the RBFN-IS . . . . .	28
5.2	Simulation results . . . . .	31
5.2.1	Lifting the payload . . . . .	33
5.2.2	Lowering the payload . . . . .	36
5.3	Chapter's Conclusion . . . . .	39
<b>CHAPTER 6: RESULTS WITH THE EXPERIMENTAL MODEL</b>		<b>40</b>
6.1	Experimental crane model . . . . .	40
6.1.1	Hardware system . . . . .	40
6.1.2	Electrical cabinet . . . . .	41
6.1.3	NI myRIO 1900 Kit . . . . .	42
6.1.4	Labview application . . . . .	44
6.2	Implementation of the control scheme for experimental model . . . . .	45
6.2.1	Designing the ADRCs . . . . .	45
6.2.2	Designing the RBFN-IS . . . . .	49
6.3	Experimental results . . . . .	52
6.3.1	Lifting the payload . . . . .	53
6.3.2	Lowering the payload . . . . .	56
6.4	Chapter's Conclusion . . . . .	59
<b>CONCLUSION</b>		<b>60</b>
<b>REFERENCE</b>		<b>61</b>
<b>REFERENCES</b>		<b>63</b>
<b>APPENDIX</b>		<b>63</b>

## **LIST OF ABBREVIATIONS**

ADRC	Active Disturbance Rejection Control
IAE	Integral Absolute Error
IS	Input Shaping
MA	Max Amplitude
PSO	Particle Swarm Optimization
RBF	Radial Basis Function
ZVD	Zero Vibration Derivative

## LIST OF FIGURES

Figure 1.1	Overhead crane system . . . . .	1
Figure 1.2	The structure of overhead crane system . . . . .	2
Figure 2.1	Modeling of crane system . . . . .	6
Figure 2.2	Simulation of crane mathematical model . . . . .	8
Figure 2.3	Driving force of trolley movement in Case 1 . . . . .	9
Figure 2.4	Driving force of cable length in Case 1 (N) . . . . .	9
Figure 2.5	Trolley position in Case 1 . . . . .	10
Figure 2.6	Cable length in Case 1 . . . . .	10
Figure 2.7	Payload sway angle in Case 1 . . . . .	11
Figure 2.8	Driving force of cable length in Case 2 . . . . .	11
Figure 2.9	Trolley position in Case 2 . . . . .	12
Figure 2.10	Cable length in Case 2 . . . . .	12
Figure 2.11	Payload sway angle in Case 2 . . . . .	13
Figure 2.12	Trolley position in Case 3 . . . . .	13
Figure 2.13	Cable length in Case 3 . . . . .	14
Figure 2.14	Payload sway angle in Case 3 . . . . .	14
Figure 3.1	Overall control structure . . . . .	16
Figure 3.2	Structure of close-loop system . . . . .	18
Figure 4.1	The system's response to sequence of pulses . . . . .	19
Figure 4.2	Structure of RBF network . . . . .	21
Figure 4.3	The structure of two implemented RBF networks . . . . .	23
Figure 4.4	General flowchart of Particle Swarm Optimization algorithm .	25
Figure 5.1	The simulation of ADRC controller . . . . .	28
Figure 5.2	The performance index during training process for (a) $t_2$ and (b) $t_3$ . . . . .	30
Figure 5.3	The simulation of overall control structure . . . . .	33
Figure 5.4	Trolley position response in Case 1 . . . . .	33
Figure 5.5	Cable length response in Case 1 . . . . .	34

Figure 5.6 Payload sway angle in Case 1 . . . . .	35
Figure 5.7 (a) Control force for trolley position in Case 1, (b) Control force for cable length in Case 1 . . . . .	36
Figure 5.8 Trolley position response in Case 2 . . . . .	36
Figure 5.9 Cable length response in Case 2 . . . . .	37
Figure 5.10 Payload sway angle in Case 2 . . . . .	38
Figure 5.11 (a) Control force for trolley position in Case 2, (b) Control force for cable length in Case 2 . . . . .	39
Figure 6.1 The experimental crane model . . . . .	40
Figure 6.2 The NI-myRIO 1900 . . . . .	42
Figure 6.3 The hardware components of the NI-myRIO 1900 Kit . . . . .	43
Figure 6.4 The I/O pins on the MSP ports . . . . .	43
Figure 6.5 The I/O pins on the MXP port . . . . .	44
Figure 6.6 The LabVIEW program for motors identification . . . . .	46
Figure 6.7 Trolley speed for different control voltages . . . . .	46
Figure 6.8 Rate of change of cable length for different control voltages . .	47
Figure 6.9 (a) ADRC controller for payload position, (b) ADRC controller for cable length . . . . .	49
Figure 6.10 Input Shaping parameters selection using the PSO algorithm .	50
Figure 6.11 The Labview program for control . . . . .	52
Figure 6.12 Experimental trolley position response in Case 1 . . . . .	53
Figure 6.13 Experimental cable length response in Case 1 . . . . .	54
Figure 6.14 Experimental payload sway angle in Case 1 . . . . .	55
Figure 6.15 (a) Control voltage for trolley position in Case 1, (b) Control voltage for cable length in Case 1 . . . . .	56
Figure 6.16 Experimental trolley position response in Case 2 . . . . .	56
Figure 6.17 Experimental cable length response in Case 2 . . . . .	57
Figure 6.18 Experimental payload sway angle in Case 2 . . . . .	58
Figure 6.19 (a) Control voltage for trolley position in Case 2, (b) Control voltage for cable length in Case 2 . . . . .	59

## LIST OF TABLES

Table 2.1	Crane system's parameters . . . . .	7
Table 5.1	Parameters of ADRCs . . . . .	27
Table 5.2	The parameters of PSO algorithm . . . . .	28
Table 5.3	Optimal Input Shaping parameters . . . . .	29
Table 5.4	Approximation errors . . . . .	31
Table 5.5	Parameters of AOF-ZVD and AOL-ZVD . . . . .	32
Table 5.6	Trolley position response in Case 1 . . . . .	33
Table 5.7	Cable length response in Case 1 . . . . .	34
Table 5.8	Payload sway angle in Case 1 . . . . .	35
Table 5.9	Trolley position response in Case 2 . . . . .	37
Table 5.10	Cable length response in Case 2 . . . . .	37
Table 5.11	Payload sway angle in Case 2 . . . . .	38
Table 6.1	The pin description of the MSP ports . . . . .	44
Table 6.2	The pin description of the MXP port . . . . .	44
Table 6.3	Parameters of ADRCs . . . . .	48
Table 6.4	Optimal Input Shaping parameters . . . . .	51
Table 6.5	Parameters of AOF-ZVD and AOL-ZVD . . . . .	53
Table 6.6	Experimental trolley position response in Case 1 . . . . .	54
Table 6.7	Experimental cable length response in Case 1 . . . . .	54
Table 6.8	Experimental payload sway angle in Case 1 . . . . .	55
Table 6.9	Experimental trolley position response in Case 2 . . . . .	57
Table 6.10	Experimental cable length response in Case 2 . . . . .	57
Table 6.11	Experimental payload sway angle in Case 2 . . . . .	58

# CHAPTER 1. INTRODUCTION

Chapter 1 will provide an introduction to the practical aspects of the overhead crane system, as well as an overview of its structure and real-world applications. Additionally, the chapter will address operational issues and describe the main objectives of this project.

## 1.1 Overview of the crane system

Among various material handling equipment, the overhead crane (Figure 1.1) is a widely used and popular device in industrial sectors, particularly in manufacturing plants, warehouses, and workshops. With its diverse configurations and designs tailored to specific tasks and loads, overhead cranes meet the demands of material transportation while ensuring efficiency and high safety standards.

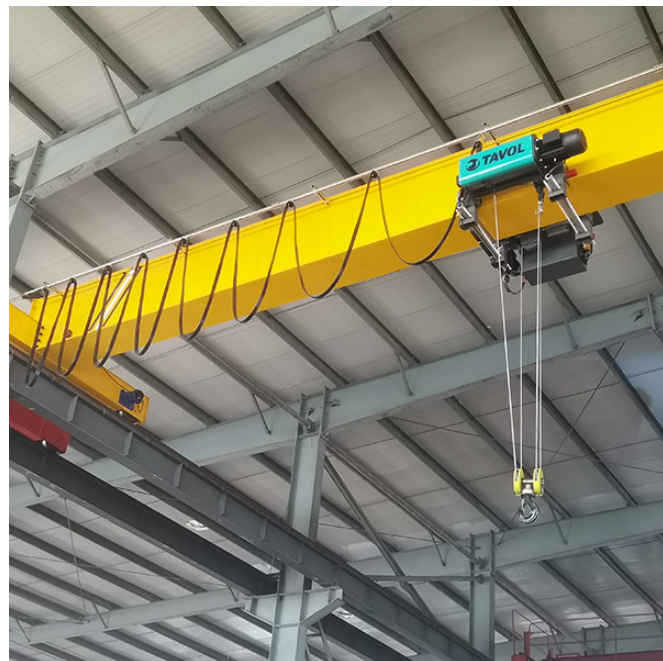


*Figure 1.1 Overhead crane system*

The overhead crane is a specialized material handling equipment used for lifting, lowering, and moving heavy and bulky objects safely and precisely. With lifting capacities ranging from 1 to 500 tons and predominantly powered by electric motors, overhead cranes optimize time and labor, thereby improving production productivity and efficiency. The elevated design of the overhead crane allows for flexible movement and creates additional storage space for goods, while ensuring the safety of operators and workers on the ground. The working principle of an overhead crane involves an electric motor transmitting motion through the drive shaft and couplings to gearboxes, which, in turn, transmit motion to the wheel assembly that moves the

entire main beam along the running girders. The hoist, which contains the lifting mechanism, travels on rails mounted on the main beam and is used to lift and lower the cargo. The crane operator utilizes the control system in the cabin to command the electric motors and apply brakes when necessary.

### **1.1.1 The structure of the crane system**

An overhead crane is a type of machinery with a steel bridge-like structure installed at an elevated position, utilizing the empty space above a workshop. It employs a dedicated rail system installed on the walls or beams of the facility for movement and transportation of goods.

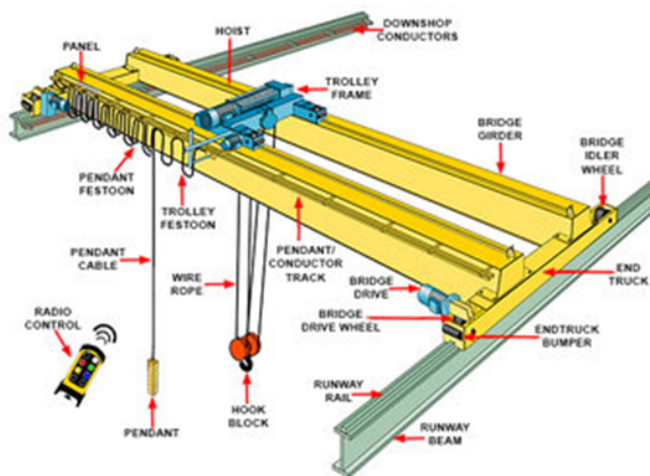


*Figure 1.2 The structure of overhead crane system*

Currently, there are numerous types of overhead cranes available in the market, but most of them share common basic components:

- Main beam: The main beam is typically designed in an I-beam shape and serves as the primary load-bearing structure of the crane. It also acts as the runway for the crane trolley, facilitating the movement and transportation of goods. The design of the main beam is carefully selected to match the lifting capacity and the distance between the end carriages, ensuring optimal strength, rigidity, and resilience.
- End carriages: The end carriages are steel structures mounted on both ends of the main beam. They are responsible for bearing the load from the crane and transferring it to the runway rails. The end carriages are usually connected to the main beam using bolts or welded joints, creating a crane bridge frame. To minimize collisions during the crane's movement to the end stop position, the ends of the main beam are equipped with dynamic traveling and rubber-damping systems.

Depending on the lifting capacity, the crane can be equipped with different-sized wheels or swiveling wheels.

- Runway rails: The runway rails are dedicated tracks installed to support the crane's movement within the workspace. They provide the path for the drive motors and wheels of the crane to operate.
- Traveling wheels and drive motors: These are crucial components that enable the crane to move and perform material handling tasks. The crane moves on four sets of wheels, two active and two passive, installed on the end carriages. The wheels are powered by motors, allowing the crane to move along the runway rails. The active and passive wheel sets have different structures and functions, tailored to their respective roles.
- Trolley: The trolley is a horizontal platform that runs along the main beam. It is equipped with lifting mechanisms that raise or lower the load.
- Hoist: This is a component mounted on the crane trolley. It consists of a motor, drum, and lifting hook, responsible for raising, holding, or lowering the load. Two main types of hoists are commonly used in overhead cranes: electric chain hoists for smaller lifting capacities (ranging from 500kg to 5 tons) and electric wire rope hoists for larger lifting capacities (ranging from 1 to tens of tons).
- Hook: The hook is a device used to secure and lift the load, either using chains or electric cables that pass over a pulley.
- Damping system: The damping system is designed to absorb the crane's energy and reduce collisions, bringing the crane to a controlled stop and minimizing forces when the crane or trolley reaches the end of its travel. Damping devices, such as bumpers, may be installed on the crane, end carriages, or runway end points.
- Control system: The control system includes the control panel or cabin, from which the operator can manage the crane's movement and lifting operations. It allows for precise and intuitive control of the crane, either through manual operation, remote control, or from the cabin.
- Electrical system: The electrical system powers the crane and includes motor controls, safety devices, and other electrical components needed for smooth and safe crane operation. The electrical components are typically housed in an electrical control panel.

### ***1.1.2 Applications of overhead crane***

The applications of overhead cranes are diverse and critical across numerous industries, providing substantial benefits in terms of increased productivity, improved safety, and cost-effective material handling solutions. Some of the key industrial applications of overhead cranes include:

- Manufacturing and Production: In manufacturing facilities, overhead cranes play a crucial role in handling raw materials, intermediate components, and finished products. They facilitate the movement of heavy machinery and enable efficient assembly and production processes.
- Construction Industry: Overhead cranes are often used in construction sites to lift and position heavy building materials, such as steel beams, concrete panels, and prefabricated structures. They enhance construction efficiency and reduce manual labor requirements.
- Warehousing and Logistics: Overhead cranes are essential for efficient warehouse operations. They enable easy loading and unloading of cargo from trucks, organize inventory in storage racks, and expedite order fulfillment processes.
- Shipbuilding and Maritime Industry: In shipyards, large overhead cranes are employed to lift ship components, engines, and sections during shipbuilding and repair operations. These cranes are capable of handling immense loads required in the maritime industry.
- Mining and Material Extraction: Overhead cranes are utilized in mines and quarries to transport heavy materials, ores, and rocks. They help in moving bulk materials from one location to another, improving mining productivity.

## **1.2 Operation problems**

During the operation of an overhead crane system, the movement of the trolley and the lifting or lowering of payloads are crucial actions that are often performed in sequence. However, to improve the system's overall productivity, it becomes advantageous to have the ability to control the movement of both the trolley and the payload simultaneously. By synchronizing these actions, the crane operator can optimize the workflow, saving time and effort in the material handling process.

One persistent challenge encountered in crane systems is the occurrence of vibrations during operation. These vibrations can arise from various sources, such as the movement of the trolley along the rails, the acceleration and deceleration of the

hoist, or external factors like wind or uneven loading. These vibrations can have detrimental effects on the system's durability and performance, leading to increased wear and tear on the components and potential safety risks. Furthermore, the presence of payload oscillations within the system can be considered as internal disturbances. These oscillations can occur due to the dynamic nature of the lifted loads, causing fluctuations in the cable length and the trolley's position. Such disturbances pose significant challenges in maintaining precise control over the crane's movements and can impact the overall accuracy and stability of the system.

To address these problems, this project will utilize the Active Disturbance Rejection Controls (ADRC) in conjunction with a Radial Basis Function network-based Input Shaping (RBFN-IS). The main objectives of this study are as follows:

- Investigate real-world overhead crane systems, obtain the mathematical models, and introduce about the experimental models for the crane system under payload hoisting process.
- Explore the concept of Active Disturbance Rejection Control and design the controllers for both the mathematical and experimental models.
- Study the Input Shaping method, Radial Basis Function network, and the Particle Swarm Optimization algorithm. Subsequently, design and train the RBFN-IS method to improve the vibration suppression capabilities of the system for both mathematical and experimental models.

### **1.3 Chapter's conclusion**

In Chapter 1, an overview of the overhead crane system was presented, covering its structure and real-world applications. Additionally, the chapter addressed operational challenges and discussed the content of the project to tackle the identified difficulties.

## CHAPTER 2: MATHEMATICAL MODEL OF CRANE SYSTEM

Chapter 2 will delve into the exploration of the mathematical model of the overhead crane system, as well as conduct tests to validate the obtained model.

### 2.1 Modeling the crane system

For modeling convenience, the following assumptions are made:

- The payload and trolley are considered point masses
- The cable's mass and elasticity are neglected
- Motions of all components are considered to lie only in the  $x - y$  plane

The dynamic model for an overhead crane encompasses the simultaneous operations of trolley movement and payload hoisting (Figure 2.1). The physical representation of this system comprises three distinct masses:  $m_p$  denoting the mass of the payload,  $m_t$  signifying the mass of the trolley, and  $m_h$  representing the mass associated with the rotating components of the payload hoisting mechanism. The position of the payload ( $x_p, y_p$ ) is given by:

$$x_p = x + l \sin \theta \quad (2.1)$$

$$y_p = -l \cos \theta \quad (2.2)$$

where  $x$  is the position of the trolley, while  $l$  is the cable length.  $\theta$  denotes the payload sway angle.

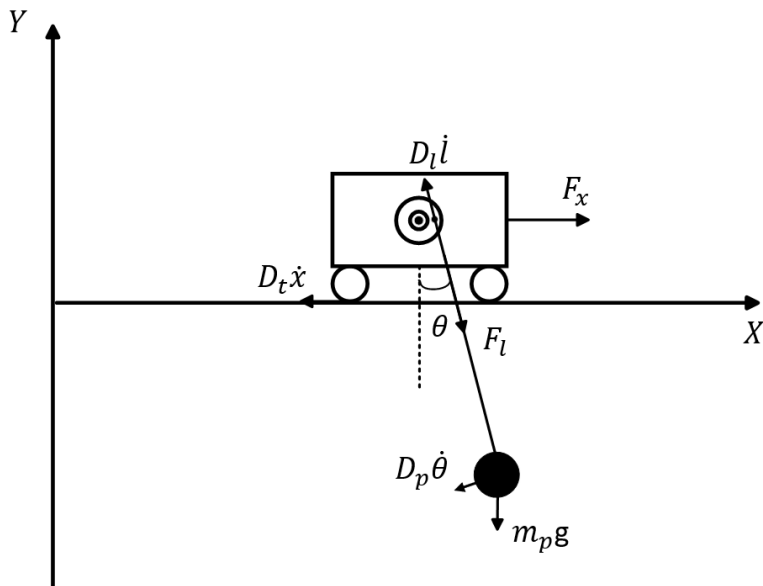


Figure 2.1 Modeling of crane system

The kinetic energy of the crane and its load and the potential energy of the payload are represented as:

$$K = \frac{1}{2} (m_t \dot{x}^2 + m_h \dot{l}^2) + \frac{m}{2} v_p^2 \quad (2.3)$$

$$P = m_p g l (1 - \cos \theta) \quad (2.4)$$

where  $g$  and  $v_p$  are the gravitational constant and the payload speed, respectively. The payload speed is described as Equation (2.5):

$$\begin{aligned} v_p^2 &= \dot{x}_p^2 + \dot{y}_p^2 \\ &= \dot{x}^2 + \dot{l}^2 + l^2 \dot{\theta}^2 + 2 (\sin \theta \dot{l} + l \cos \theta \dot{\theta}) \dot{x} \end{aligned} \quad (2.5)$$

The Lagrangian  $L$  and the Rayleigh's dissipation function  $F$  are defined as:

$$L = K - P = \frac{1}{2} (m_t \dot{x}^2 + m_h \dot{l}^2) + \frac{m}{2} v_p^2 - m_p g l (1 - \cos \theta) \quad (2.6)$$

$$F = \frac{1}{2} (D_t \dot{x}^2 + D_l \dot{l}^2 + D_p \dot{\theta}^2) \quad (2.7)$$

where  $D_t$ ,  $D_l$  and  $D_p$  are the viscous damping coefficients associated with the  $x$ ,  $l$  and swing motions, respectively. By substituting  $L$  and  $F$  into Lagrange's equations associated with the generalized coordinates  $\mathbf{q} = [x \ l \ \theta]^T$ , the dynamic model of the crane system is obtained as follow:

$$\begin{aligned} (m_t + m_p) \ddot{x} + m_p l \cos \theta \ddot{\theta} + m_p \sin \theta \ddot{l} + D_t \dot{x} + 2m_p \cos \theta \dot{l} \dot{\theta} - m_p l \sin \theta \dot{x}^2 &= F_x \\ (m_h + m_p) \ddot{l} + m_p \sin \theta \ddot{x} + D_l \dot{l} - m_p l \dot{\theta}^2 - m_p g \cos \theta &= F_l \\ m_p l^2 \ddot{\theta} + m_p l \cos \theta \ddot{x} + 2m_p l \dot{l} \dot{\theta} + m_p g l \sin \theta + D_p \dot{\theta} &= 0 \end{aligned} \quad (2.8)$$

where  $F_x$  represents the driving force that facilitates the linear movement of the trolley, while  $F_l$  is the force primarily employed for hoisting the payload. The parameters of the simulation crane model are chosen as in Table 2.1.

*Table 2.1 Crane system's parameters*

Parameter	Value
Payload mass, $m_p$	0.5 - 1.5 kg
Trolley mass, $m_t$	4 kg
Hoisting component mass, $m_h$	3 kg
Damping coefficients, $D_t, D_l$	25, 55 Ns/m
Swing damping coefficient, $D_p$	0.1 Ns/rad
Cable length, $l$	0.1 - 0.8 m
Gravitational constant, $g$	$9.81 \text{ ms}^{-2}$

## 2.2 Verifying the mathematical model

The obtained mathematical model (2.8) will be simulated using MATLAB/Simulink, as shown in Figure 2.2. In the simulation, the variables  $x_1$ ,  $x_3$ , and  $x_5$  represent the trolley displacement, cable length, and payload's sway angle, respectively. At the initial state, when  $x(0) = 0$  and  $\theta(0) = 0$ , it is necessary for the cable length to be greater than 0. Additionally, based on the dynamic model, the driving force  $F_l$  at the initial state must have the same magnitude but opposite direction to the weight of the payload, ensuring that the system is in equilibrium. To validate the mathematical model, several test scenarios will be performed:

- (i) Considering only the force  $F_x$ .
- (ii) Considering only the force  $F_l$ .
- (iii) Initial payload sway angle is non-zero.

The model parameters will be obtained from Table 2.1. The payload mass and initial cable length are  $m_p = 0.5$  kg and  $l = 0.6$  m, respectively.

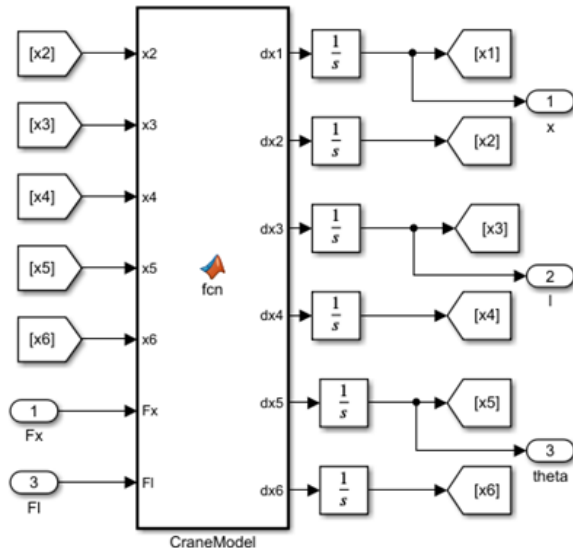


Figure 2.2 Simulation of crane mathematical model

- Case 1: Considering only the force  $F_x$

We will apply a constant force  $F_x = 15$  N (Figure 2.3) to initiate translational motion of the trolley along the  $x$ -axis while keeping  $F_l$  at a constant value of  $-m_p g = -4.905$  N (Figure 2.4). As shown in Figure 2.5, initially, when the propelling force  $F_x$  is applied, the trolley will undergo an accelerating motion and then transition into a steady

motion along the positive  $x$ -axis. From Figure 2.7, it is evident that the trolley's initial motion induces oscillations in the payload. Additionally, these payload oscillations affect the cable length, causing it to decrease from its initial position (Figure 2.6). The magnitude of the payload oscillations determines the extent of this change.

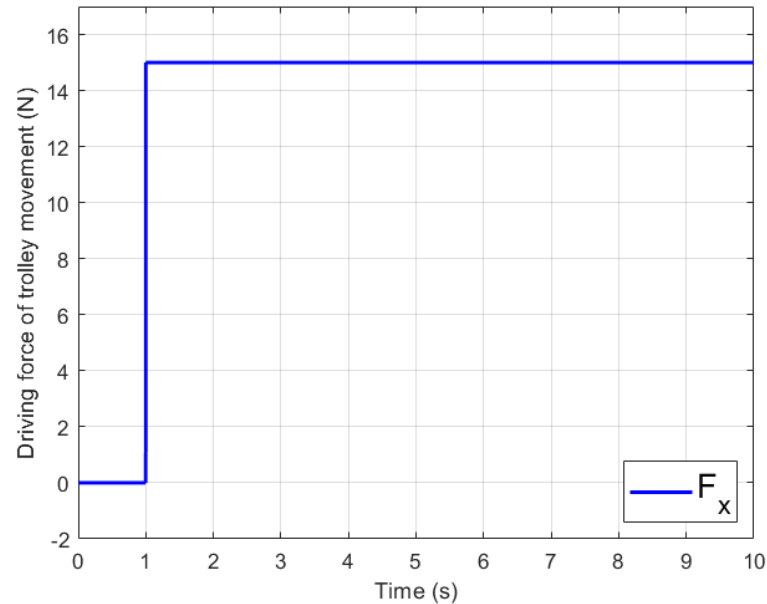


Figure 2.3 Driving force of trolley movement in Case 1

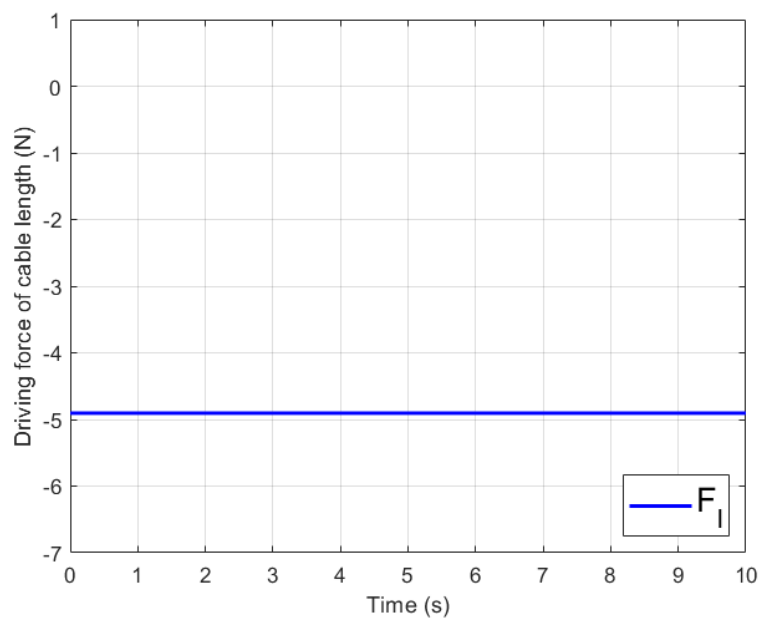


Figure 2.4 Driving force of cable length in Case 1 (N)

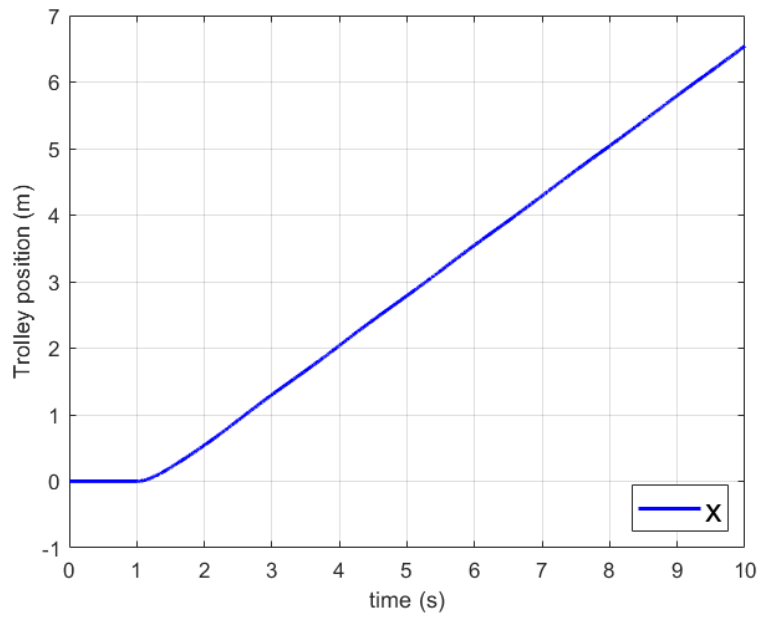


Figure 2.5 Trolley position in Case 1

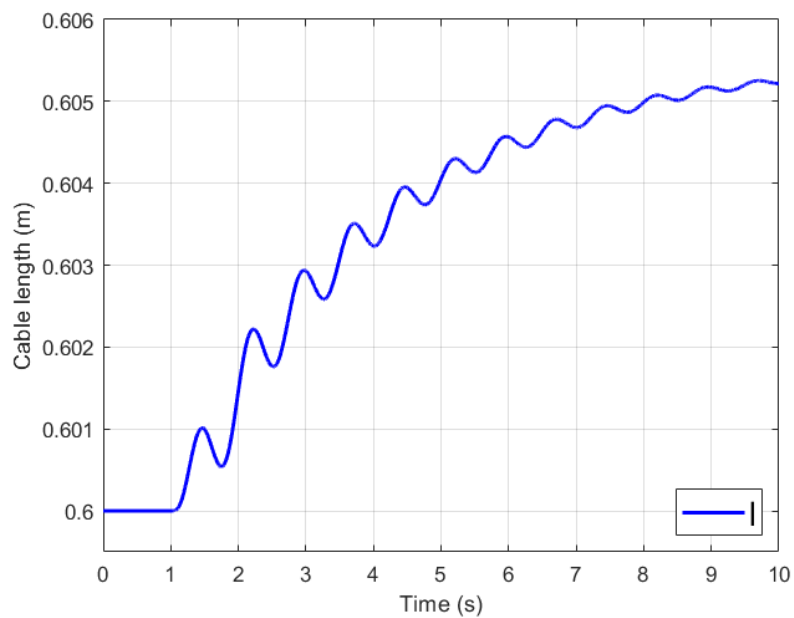


Figure 2.6 Cable length in Case 1

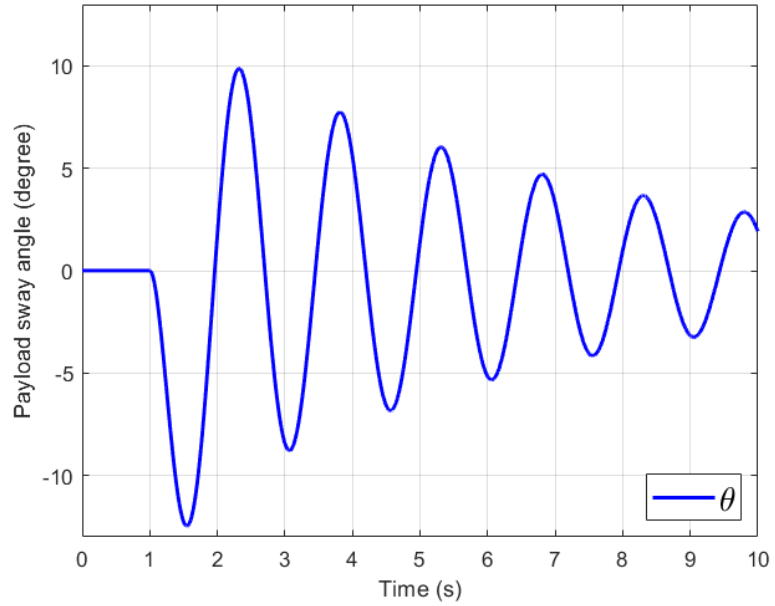


Figure 2.7 Payload sway angle in Case 1

- Case 2: Considering only the force  $F_l$

In this case, we will lower the payload from its initial position at 0.6m and then raise it by applying the force  $F_l$  over time, as shown in Figure 2.8. The force  $F_x$  is kept to a constant value of 0 N. Initially, the payload is lowered and then transitions into a lifting motion along the y-axis, as illustrated in Figure 2.10. Figures 2.9 and 2.11 demonstrate that the hoisting motion of the payload does not affect the trolley displacement or induce any oscillations in the payload.

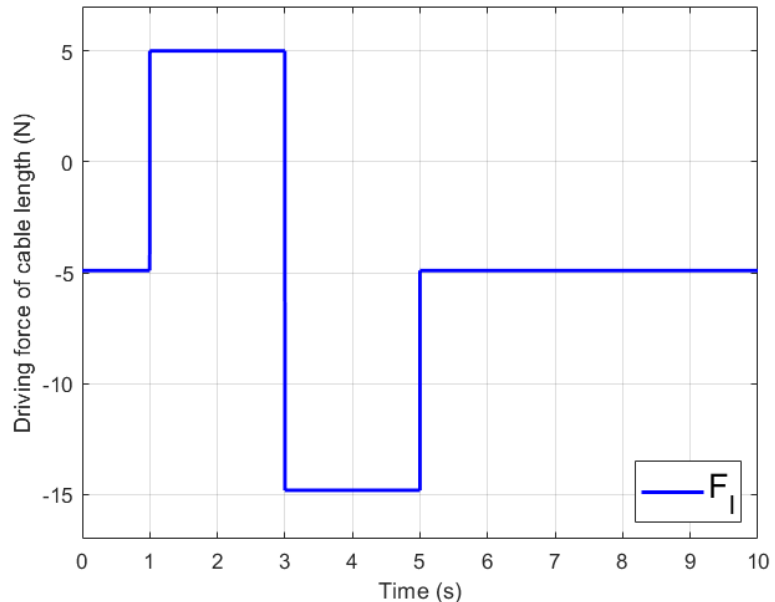


Figure 2.8 Driving force of cable length in Case 2

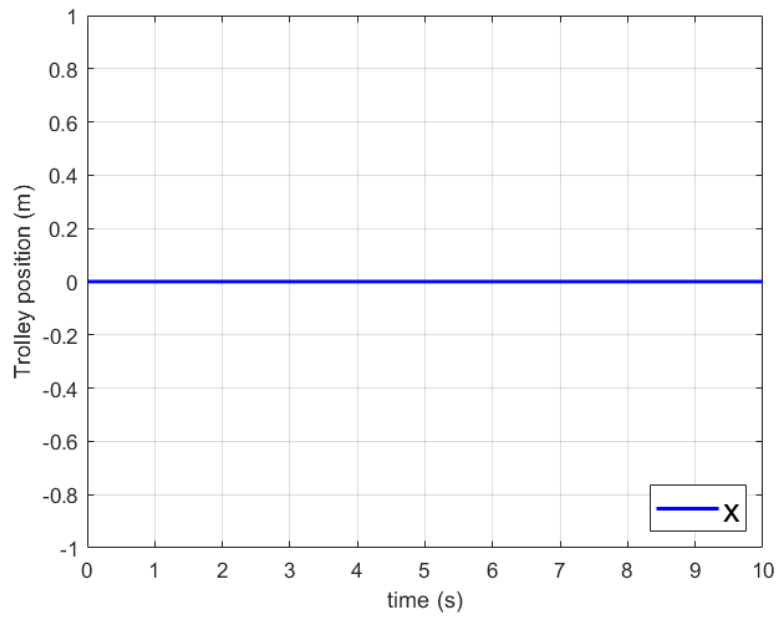


Figure 2.9 Trolley position in Case 2

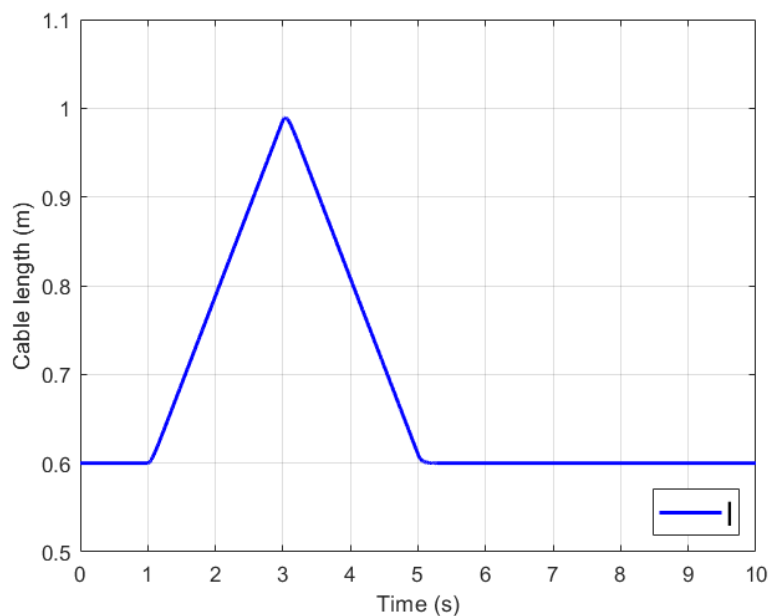
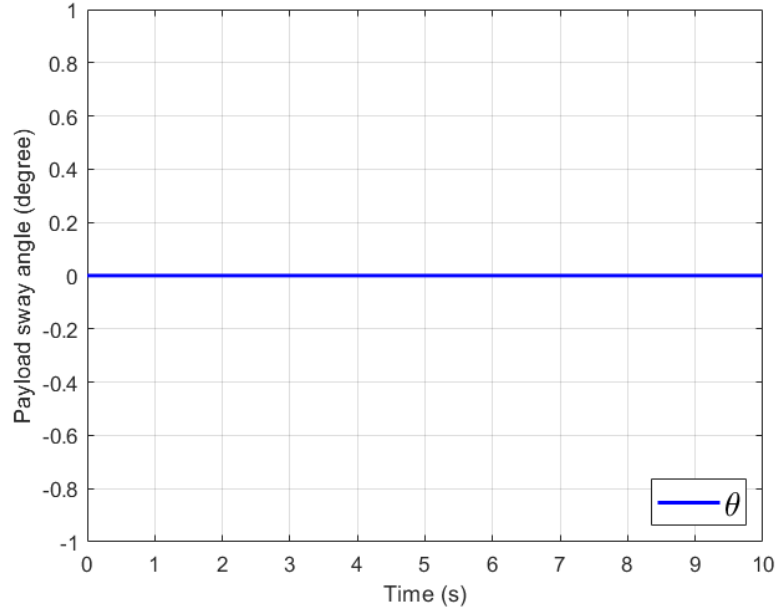


Figure 2.10 Cable length in Case 2



*Figure 2.11 Payload sway angle in Case 2*

- Case 3: The initial payload sway angle is non-zero

At the initial state, the payload will be positioned such that the angle between the cable and the vertical axis is  $\theta = 10$  degrees. Subsequently, the payload will be released to oscillate, as depicted in Figure 2.14. From Figures 2.12 and 2.13, it is evident that the payload oscillations have an impact on both the trolley's position and the cable length. The magnitude of this effect is more pronounced with larger payload oscillations.  $F_x$  and  $F_l$  are kept at constant values of 0 N and -4.905 N, respectively.

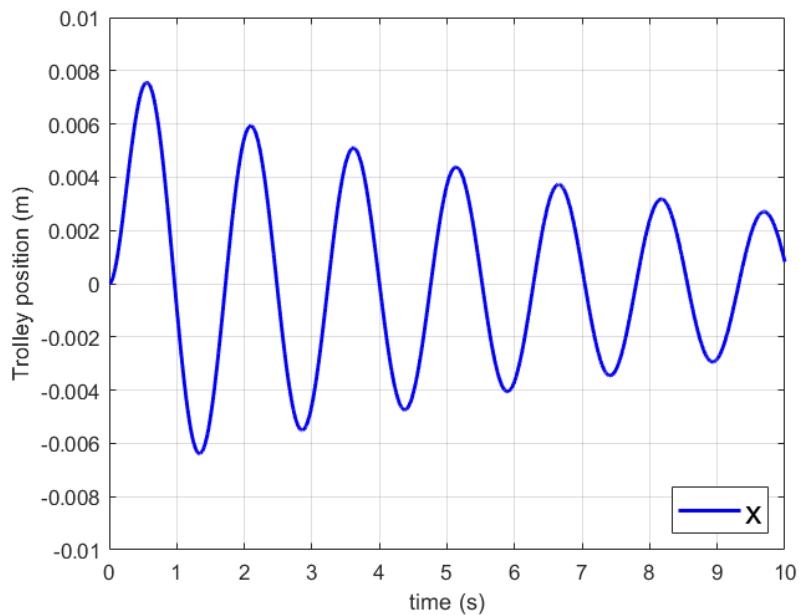


*Figure 2.12 Trolley position in Case 3*

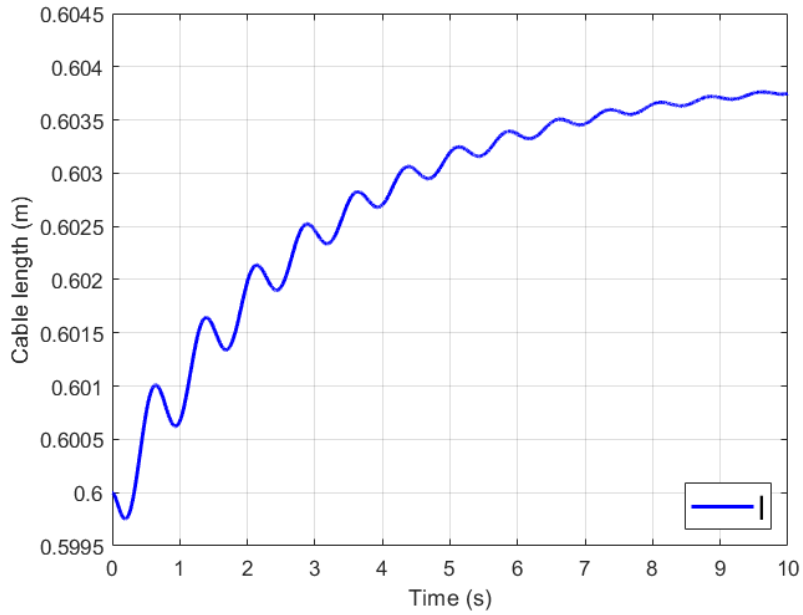


Figure 2.13 Cable length in Case 3

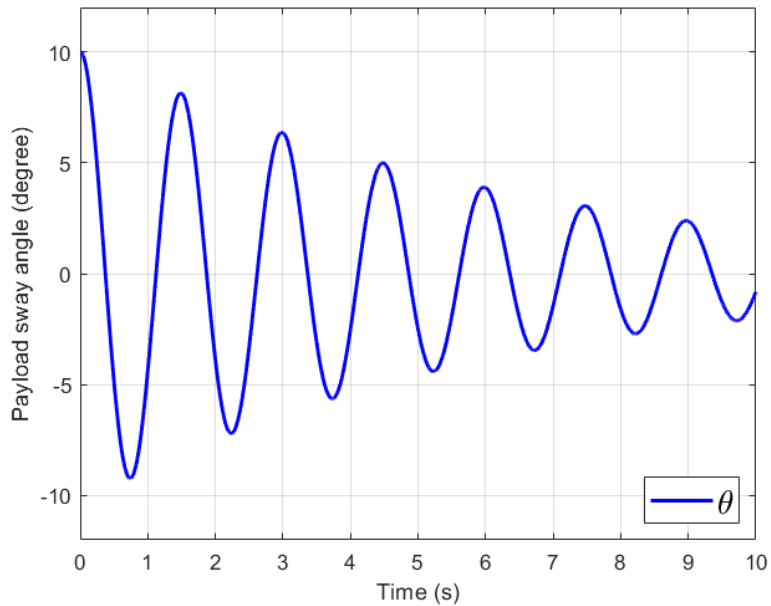


Figure 2.14 Payload sway angle in Case 3

### 2.3 Chapter's conclusion

In Chapter 2, the task of modeling the overhead crane system was undertaken, encompassing the translational motion of the trolley as well as the hoisting process of the payload. Furthermore, a series of simulation scenarios have been executed to examine the validity of the derived dynamic model.

## CHAPTER 3: ACTIVE DISTURBANCE REJECTION CONTROL

Chapter 3 will present an overview of the control structure of the system, as well as the theoretical foundations of Active Disturbance Rejection Control.

### 3.1 Control structure

The overall control structure can be depicted in Figure 3.1, featuring two separate closed-loop control systems to regulate the position of the trolley and the cable length. Based on the results obtained in Part (2.2) and the dynamic model of the crane system, it becomes apparent that the oscillations experienced by the load have a direct impact on both its positional displacement and the length of the cable. These influences can be regarded as internal disturbances within the system. To effectively counteract the adverse effects of these disturbances and ensure a robust and streamlined design, the study employed two distinct Active Disturbance Rejection Controls with the objective of rejecting and attenuating the impact of load oscillations. The ADRCs operate independently, each generating a unique control signal. One controller focuses on regulating the driving force  $F_x$ , responsible for governing the translational motion of the trolley, while the other controller is responsible for controlling the force  $F_l$ , predominantly employed for lifting and lowering the payload.

To address vibration suppression, the positioning control loop incorporates a feed-forward technique, namely Radial Basis Function network-based Input Shaping. The Input Shaping method involves convolving the desired signal with a sequence of pulses characterized by specific amplitudes and time durations. This shaping process effectively modifies the command input to the system, mitigating undesired vibrations and improving overall performance. The RBF network plays a crucial role by adaptively updating the parameters of the Input Shaping technique based on the current cable length and payload mass. This adaptive adjustment ensures that the system can dynamically respond to changing operating conditions, resulting in efficient vibration suppression during crane operations.

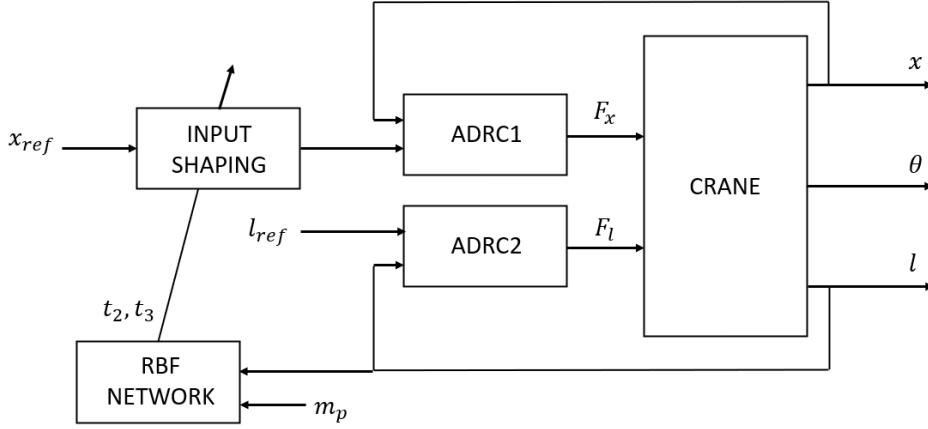


Figure 3.1 Overall control structure

### 3.2 Concept of ADRC

Active Disturbance Rejection Control, initially proposed by J. Han in 2009 [1], is an advanced control technique that has gained significant attention due to its robustness and effectiveness in handling complex control problems. Instead of relying on a detailed model, ADRC focuses on the direct estimation and cancellation of disturbances that affect the system. Consider a second-order system of the form [2]:

$$\ddot{y}(t) = f(t, \dot{y}, y, \omega) + b_0 u(t) \quad (3.1)$$

where  $y(t)$  represents the output while  $u(t)$  is the control signal and  $f(t)$  is general disturbances. The control constant is denoted as  $b_0$ .

The idea behind ADRC is to use an Extended State Observer (ESO) to estimate the total disturbance in the system. It treats disturbances as part of the system's extended state; thereby, the ESO can estimate their values and compensate for their effects in real time. The ESO is constructed based on an extended state-space model. With states  $x_1, x_2$  representing  $y$  and  $\dot{y}$ , respectively, while  $x_3 = f$  is the augmented state, the extended model of the differential equation (3.1) can be expressed as:

$$\begin{pmatrix} \dot{x}_1(t) \\ \dot{x}_2(t) \\ \dot{x}_3(t) \end{pmatrix} = \underbrace{\begin{pmatrix} 0 & 1 & 0 \\ 0 & 0 & 1 \\ 0 & 0 & 0 \end{pmatrix}}_A \begin{pmatrix} x_1(t) \\ x_2(t) \\ x_3(t) \end{pmatrix} + \underbrace{\begin{pmatrix} 0 \\ b_0 \\ 0 \end{pmatrix}}_B u(t) + \begin{pmatrix} 0 \\ 0 \\ 1 \end{pmatrix} \dot{f}(t) \quad (3.2)$$

$$y(t) = \underbrace{\begin{pmatrix} 1 & 0 & 0 \end{pmatrix}}_C \begin{pmatrix} x_1(t) \\ x_2(t) \\ x_3(t) \end{pmatrix}$$

The ESO can be represented as Equation (3.3):

$$\begin{pmatrix} \dot{x}_1(t) \\ \dot{x}_2(t) \\ \dot{x}_3(t) \end{pmatrix} = \begin{pmatrix} 0 & 1 & 0 \\ 0 & 0 & 1 \\ 0 & 0 & 0 \end{pmatrix} \begin{pmatrix} \hat{x}_1(t) \\ \hat{x}_2(t) \\ \hat{x}_3(t) \end{pmatrix} + \begin{pmatrix} 0 \\ b_0 \\ 0 \end{pmatrix} u(t) + \begin{pmatrix} l_1 \\ l_2 \\ l_3 \end{pmatrix} (y(t) - \hat{x}_1(t)) \quad (3.3)$$

$$= \underbrace{\begin{pmatrix} -l_1 & 1 & 0 \\ -l_2 & 0 & 1 \\ -l_3 & 0 & 0 \end{pmatrix}}_{\mathbf{A}-\mathbf{LC}} \underbrace{\begin{pmatrix} \hat{x}_1(t) \\ \hat{x}_2(t) \\ \hat{x}_3(t) \end{pmatrix}}_{\mathbf{B}} + \underbrace{\begin{pmatrix} 0 \\ b_0 \\ 0 \end{pmatrix}}_{\mathbf{L}} u(t) + \underbrace{\begin{pmatrix} l_1 \\ l_2 \\ l_3 \end{pmatrix}}_{\mathbf{L}} y(t) \quad (3.4)$$

where  $l_1$ ,  $l_2$ , and  $l_3$  are parameters of the ESO that ensure the estimation of  $y$ ,  $\dot{y}$ , and  $f$  through the corresponding  $\hat{x}_1$ ,  $\hat{x}_2$ , and  $\hat{x}_3$ .

The control signal  $u(t)$  will be constructed based on a modified PD controller.

$$u(t) = \frac{u_0(t) - \hat{f}(t)}{b_0} \quad (3.5)$$

with  $u_0(t) = K_P(r(t) - \hat{y}(t)) - K_D\dot{\hat{y}}(t)$  where  $r(t)$  is the setpoint. Subsequently, the differential equation of the system (3.1) will be transformed into:

$$\ddot{y}(t) \approx u_0 = K_P(r(t) - \hat{y}(t)) - K_D\dot{\hat{y}}(t) = K_P(r - \hat{x}_1) - K_D\hat{x}_2 \quad (3.6)$$

Applying the Laplace transform to the Equation (3.6), we obtain the transfer function for the closed-loop system as follows:

$$G_{CL}(s) = \frac{Y(s)}{R(s)} = \frac{K_P}{s^2 + K_D s + K_P} \quad (3.7)$$

The structure of the close-loop system utilizing ADRC can be depicted in Figure 3.2. The parameters of the ADRC controller are computed by tuning the closed-loop transfer function to achieve a desired transfer function of the form:  $G_{CL}(s) = \frac{s_{CL}^2}{(s-s_{CL})^2}$ . By selecting a desired 2% settling time  $T_{settle}$  for a step impulse input signal, the closed-loop poles will have the following values [2]:

$$s_{CL} \approx -\frac{5.85}{T_{settle}} \quad (3.8)$$

In order to transform the transfer function (3.7) into the desired form, the parameters  $K_P$  and  $K_D$  need to be set as follows:

$$K_P = s_{CL}^2, K_D = -2s_{CL} \quad (3.9)$$

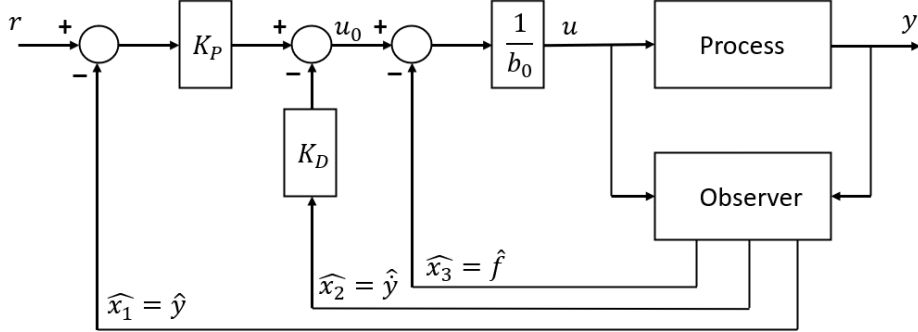


Figure 3.2 Structure of close-loop system

The dynamics of the observer need to be selected to ensure that they are sufficiently fast to precisely track the system variations and disturbances. Therefore, the observer's poles will be set to coincide with each other and be positioned to the left of the closed-loop poles.

$$s_{ESO1,2} = s_{ESO} \approx k_{ESO}s_{CL} = (3\dots10)s_{CL} \quad (3.10)$$

The observer gains are computed based on the desired eigenvalues of the characteristic polynomial of the  $(\mathbf{A} - \mathbf{LC})$  matrix. By selecting appropriate eigenvalues, the response of the observer can be shaped to achieve the desired accuracy in disturbance estimation and control performance. Following the bandwidth-parameterization method [3], the eigenvalues are assigned as the poles of the observer  $s_{ESO}$ .

$$\det(s\mathbf{I} - (\mathbf{A} - \mathbf{LC})) = s^3 + l_1s^2 + l_2s + l_3 = (s - s_{ESO})^3 \quad (3.11)$$

The solutions for  $l_1$ ,  $l_2$ , and  $l_3$  are obtained as:

$$l_1 = -3s_{ESO}, l_2 = 3s_{ESO}^2, l_3 = -s_{ESO}^3 \quad (3.12)$$

It can be easily recognizable that the parameters of the ADRC can be readily fine-tuned by selecting appropriate values for the desired settling time  $T_{settle}$  and the gain of the observer poles  $k_{ESO}$ .

### 3.3 Chapter's Conclusion

In Chapter 3, an exploration of the control structure of the system was conducted, alongside a presentation of the concept of Active Disturbance Rejection Control.

## CHAPTER 4: RADIAL BASIS FUNCTION-BASED INPUT SHAPING

Chapter 4 will introduce the theory of the Input Shaping method, as well as the structure of the Radial Basis Function network and the Particle Swarm Optimization algorithm that will be employed in this project.

### 4.1 Concept of Input Shaping

Input Shaping, initially proposed by Singer and Seering [4], is a feed-forward technique utilized in control systems to mitigate the effects of unwanted oscillations and vibrations induced by input commands or disturbances. When an input pulse is applied to a system, the system's output tends to exhibit a decaying oscillatory response. The concept of vibration suppression for a system based on the Input Shaping method involves generating a second pulse signal with appropriate magnitude and timing to cancel out the oscillations induced by the first pulse signal, thereby effectively attenuating the overall system oscillation (Figure 4.1). This technique relies on accurately characterizing the system's dynamics and appropriately selecting shaping parameters to achieve the desired control objectives.

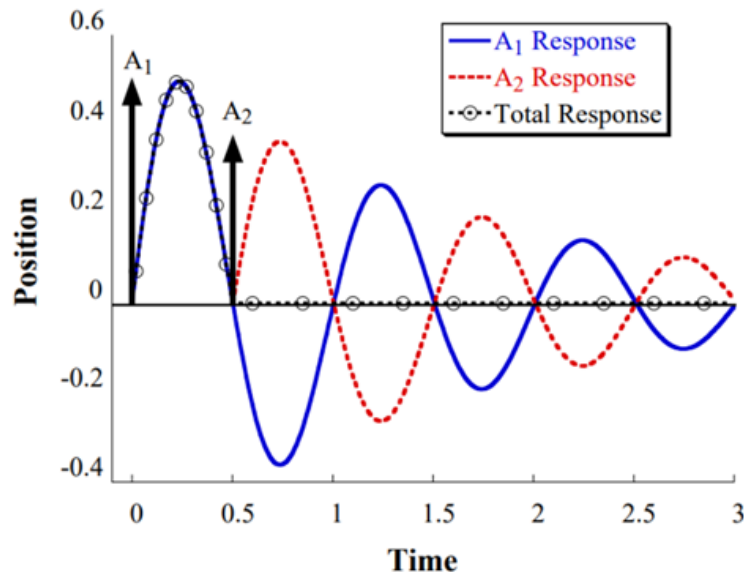


Figure 4.1 The system's response to sequence of pulses

Considering a system with a natural frequency  $\omega_n$  and damping ratio  $\xi$ , we can describe the residual oscillation caused by the sequence of input pulses as follows [5]:

$$V(\omega_n, \xi) = e^{-\xi \omega_n t_n} \sqrt{C(\omega_n, \xi)^2 + S(\omega_n, \xi)^2} \quad (4.1)$$

where:

$$C(\omega_n, \xi) = \sum_n^{i=1} A_i e^{\xi \omega_n t_i} \cos(\sqrt{1 - \xi^2} t_i)$$

$$S(\omega_n, \xi) = \sum_n^{i=1} A_i e^{\xi \omega_n t_i} \sin(\sqrt{1 - \xi^2} t_i)$$

with  $A_i$  and  $t_i$  are the magnitude and timing of the pulses, while  $n$  denotes the number of pulses in the sequence. Equation (4.1) represents the residual oscillation ratio, which quantifies the dynamic response generated by input signals relative to a single input pulse. Setting (4.1) to zero, we can determine the precise magnitude and timing of the input pulse required to eliminate the residual oscillation. By adding constraints to avoid the impulses from reaching infinite or zero values and improve the robustness of the Input Shaper, the Zero Vibration Derivative (ZVD) can be obtained as:

$$\begin{bmatrix} t_i \\ A_i \end{bmatrix} = \begin{bmatrix} 0 & T & 2T \\ \frac{1}{(1+K)^2} & \frac{2K}{(1+K)^2} & \frac{K^2}{(1+K)^2} \end{bmatrix} \quad (4.2)$$

where:

$$K = e^{-\frac{\xi \pi}{\sqrt{1-\xi^2}}} \quad (4.3)$$

$$T = \frac{\pi}{\omega_n \sqrt{1 - \xi^2}} \quad (4.4)$$

It is evident that the parameters of the traditional ZVD are closely linked to the system's natural frequency ( $\omega_n$ ) and damping ratio ( $\xi$ ). However, accurately determining these parameters can be challenging, and inaccurate computations may lead to ineffective vibration suppression. This becomes particularly significant when the cable length is continuously adjusted during the hoisting process, and there are variations in the payload mass, as these factors directly impact the system's vibration suppression capabilities. Therefore, in this project, an Input Shaping method based on the concept of ZVD technique will be employed. This method incorporates adaptively updated parameters, considering the variations in the system's parameters. By dynamically adjusting the parameters based on the system's parameter variations, it aims to achieve effective vibration suppression while maintaining the desired dynamic response. The employed Input Shaper in this project will take the following form:

$$\begin{bmatrix} t_i \\ A_i \end{bmatrix} = \begin{bmatrix} 0 & t_2 & t_3 \\ 0.25 & 0.5 & 0.25 \end{bmatrix} \quad (4.5)$$

In this context, the amplitudes of the pulses will be kept fixed to ensure the constraint  $\sum A_i = 1$  is satisfied. Meanwhile, the timings of the second pulse  $t_2$  and the third pulse  $t_3$  will be updated based on the measured cable length and payload's mass.

## 4.2 Radial Basis Function Network

The Radial Basis Function (RBF) network will be utilized to update the parameters for Input Shaping. RBF networks, introduced in 1988 [6], have garnered significant attention in various fields due to their ability to effectively approximate complex nonlinear relationships and their demonstrated success in diverse domains. The RBF network is comprised of three main layers: the input layer, the hidden layer, and the output layer (Figure 4.2).

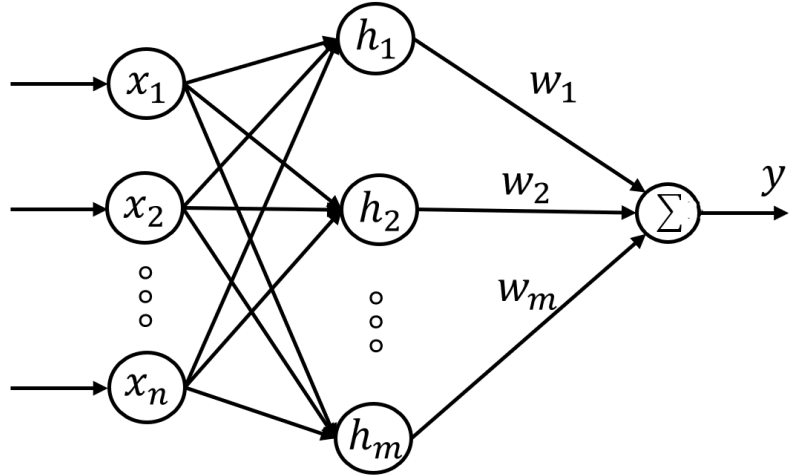


Figure 4.2 Structure of RBF network

The input layer of an RBF network receives input variables or features, representing the data to be processed by the network. Each node in the input layer corresponds to an input variable, with the number of nodes matching the number of input features. The input vector of  $n$  input nodes is denoted as  $\mathbf{x} = [x_i]^T$  ( $i = 1, 2, \dots, n$ ).

The hidden layer is responsible for the nonlinear mapping and feature extraction within the RBF network. Each radial basis function is associated with a center point  $\mathbf{c}_j$  in the input space. The activation value of each radial basis function  $h_j$  is determined by a kernel function, which calculates the distance between the input data and its corresponding center using a specified distance metric, such as Euclidean distance. The width  $b_j$  of the radial basis functions defines the influence region around each center. The activation value of each hidden node, represented in the form of a Gaussian function, is computed as follows:

$$h_j(t) = \exp\left(-\frac{\|\mathbf{x}(t) - \mathbf{c}_j(t)\|}{2b_j^2}\right), \quad j = 1, \dots, m \quad (4.6)$$

where  $m$  represents the number of hidden nodes, while  $\mathbf{c}_j = [c_{j1}, \dots, c_{jn}]$  is the center of neural net  $j$ .

The output layer of the RBF network integrates the activations of the radial basis functions from the hidden layer to generate the final output of the network. The activations from the hidden layer are weighted and combined to compute the output value, following the Equation (4.7):

$$y(t) = \sum_{j=1}^m w_j h_j \quad (4.7)$$

where  $w_j$  denotes the weight associated with the connection between the  $j$ th hidden node and the output node.

The RBF network will be trained using a labeled dataset where the parameters of the Input Shaping are the target values for each input. The optimal values for the network's parameters, including the center points, widths, and weights of the radial basis functions, will be obtained through the gradient descent method [7]. The objective of the training is to minimize the discrepancy between the predicted outputs and the desired outputs for the given training dataset. The effectiveness of the network's training and its predictive capability is given by the equation:

$$E(t) = \frac{1}{2} (yd(t) - y(t))^2 \quad (4.8)$$

where the terms  $y(t)$  and  $yd(t)$  denote the output of RBF network and target outputs, respectively. The parameters can be updated as follow.

- Weights update:

$$\Delta w_j(t) = -\eta \frac{\partial E}{\partial w_j} = \eta (yd(t) - y(t)) h_j \quad (4.9)$$

$$w_j(t) = w_j(t-1) + \Delta w_j(t) + \alpha (w_j(t-1) - w_j(t-2)) \quad (4.10)$$

- Centers update:

$$\Delta c_{ji} = -\eta \frac{\partial E}{\partial c_{ji}} = \eta (yd(t) - y(t)) w_j \frac{x_j - c_{ji}}{b_j^2} \quad (4.11)$$

$$c_{ji}(t) = c_{ji}(t-1) + \Delta c_{ji} + \alpha (c_{ji}(t-1) - c_{ji}(t-2)) \quad (4.12)$$

- Widths update:

$$\Delta b_j = -\eta \frac{\partial E}{\partial b_j} = \eta (yd(t) - y(t)) w_j h_j \frac{\|x - \mathbf{c}_j\|^2}{b_j^3} \quad (4.13)$$

$$b_j(t) = b_j(t-1) + \Delta b_j + \alpha (b_j(t-1) - b_j(t-2)) \quad (4.14)$$

where  $\eta \in (0, 1)$  represents the learning rate, while  $\alpha \in (0, 1)$  is momentum factor. In RBF network approximation, the parameters  $c_j$  and  $b_j$  must be carefully selected based on the range of the input values. Inappropriate choices of these parameters can lead to ineffective mapping of the Gaussian function, rendering the RBF network ineffective.

Due to the continuous variation of cable length during operation, the timings of the second pulse  $t_2$  and the third pulse  $t_3$  will be approximated independently for varying cable lengths and payload masses  $m_p$ . To ensure simplicity in deployment and training, this project utilizes two separate RBF networks. Both networks will share the same inputs, which are the cable length  $l$  and the payload mass  $m_p$ , directly measured from the system. One network will approximate the value of  $t_2$ , while the other network will approximate the value of  $t_3$ . Both networks will have an identical structure, consisting of 2 input layer nodes, 5 hidden layer nodes, and 1 output layer node, as illustrated in Figure 4.3.

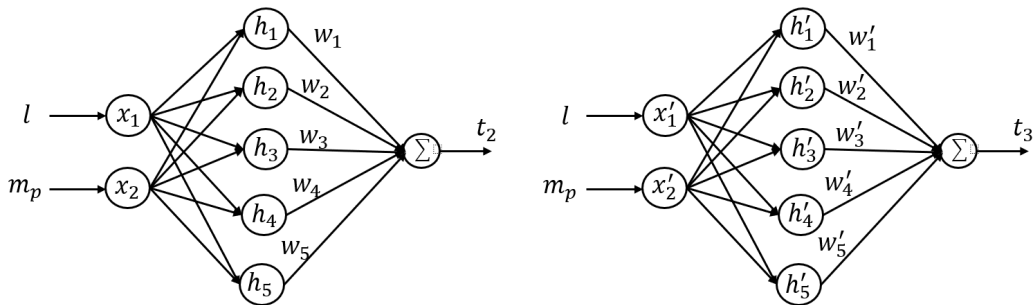


Figure 4.3 The structure of two implemented RBF networks

### 4.3 Particle Swarm Optimization

The dataset used to train the RBF network will be obtained by utilizing the Particle Swarm Optimization (PSO) algorithm. The PSO algorithm, introduced by Kennedy and Eberhart in 1995 [8], is a heuristic optimization technique that mimics the gathering behavior of bird flocks or fish schools. PSO is inspired by the idea that individuals in a population can learn from each other's experiences to find an optimal solution. In the algorithm, each particle represents a potential solution to the optimization problem. During the optimization process, each particle adjusts its position based on its own previous best solution ***pbest*** and the global best solution ***gbest*** found by any particle in the population. The personal best value ***pbest*** is determined by evaluating the fitness function for the particle's current position. For a minimization problem, a lower fitness value indicates a better solution, so the personal best is updated if the new fitness is lower than the current value. After evaluating the fitness values of all particles in an iteration, the global best value ***gbest*** is determined as the

optimal value selected from the entire population. The position and velocity of each agent are iteratively updated based on the following formulas:

$$\mathbf{v}_i^{k+1} = w\mathbf{v}_i^k + c_1 r_1 (\mathbf{pbest}_i^k - \mathbf{x}_i^k) + c_2 r_2 (\mathbf{gbest}_i^k - \mathbf{x}_i^k) \quad (4.15)$$

$$\mathbf{x}_i^{k+1} = \mathbf{x}_i^k + \mathbf{v}_i^{k+1} \quad (4.16)$$

where the terms  $r_1$  and  $r_2$  represent uniformly distributed random variables that fall within the range of (0,1). The influence of best-known personal and global position on the movement of particles is determined by acceleration factors  $c_1$ ,  $c_2$ , respectively. The velocity of each particle is updated by combining its previous velocity, its cognitive component (which is the particle's tendency to move towards its own best solution), and its social component (which is the particle's tendency to move towards the global best solution). The position of each particle is then updated based on its new velocity.

According to [9], gradually reducing the inertia weight  $w$  in each iteration enables comprehensive exploration of the search space during the initial stages and improves the convergence towards the global optimal solution in later process. The inertial weight is expressed as:

$$w = w_{max} - \frac{w_{max} - w_{min}}{MaxIter} iter \quad (4.17)$$

where  $w_{max}$  and  $w_{min}$  represent the initial and final values of the inertia weight, set to 0.9 and 0.4, respectively,  $iter$  is the current iteration number and  $MaxIter$  is the maximum number of interactions specified for the algorithm. The general flowchart of the PSO algorithm can be depicted in Figure 4.4.

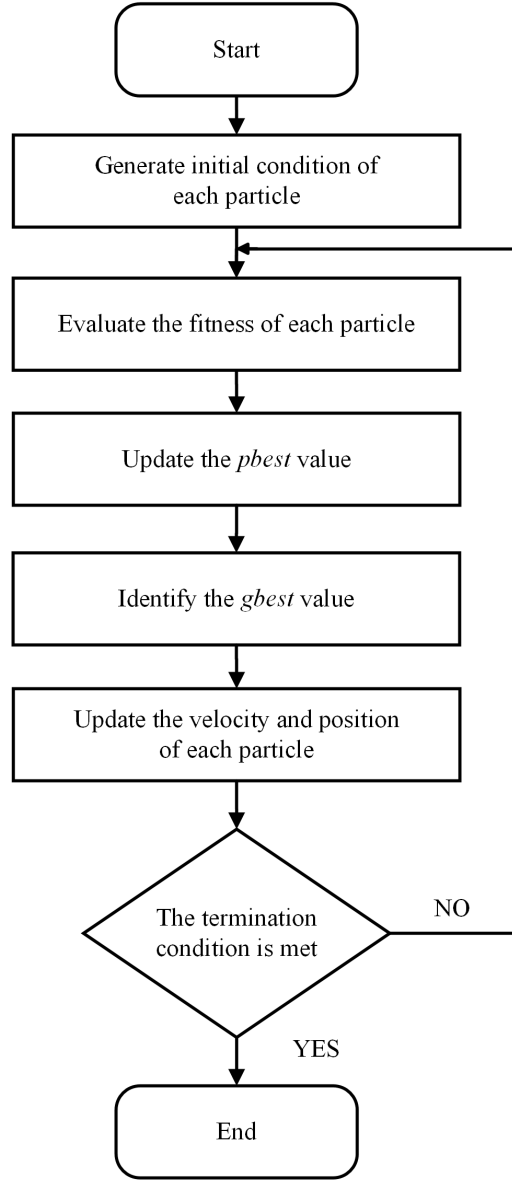


Figure 4.4 General flowchart of Particle Swarm Optimization algorithm

By examining Equations (4.5), we can observe that the PSO algorithm can be utilized to search for the parameters  $t_2$  and  $t_3$  for specific cable length and payload's mass. In order to assess the viability of candidate solutions, the fitness function employed encompasses a combination of the Integrated Absolute Error (IAE) and the maximum amplitude (MA) of payload angle error. This composite fitness function is formulated as follows:

$$J(t) = \int_0^{\infty} \eta_1 |e(t)| dt + \eta_2 MA \quad (4.18)$$

where  $e(t)$  is the error of the payload swing angle with the desired value of 0 degrees. The terms  $\eta_1$  and  $\eta_2$  represent weighted factors that capture the relationship between the IAE value and MA. It is apparent that a smaller value of the fitness function indicates a more effective vibration suppression capability of the Input Shaping

technique.

#### **4.4 Chapter's Conclusion**

Chapter 4 has presented the theoretical foundations of the Input Shaping method. Additionally, the chapter offers insights into the structure of the Radial Basis Function (RBF) network and outlines the application of both the RBF network and the Particle Swarm Optimization (PSO) algorithm within the framework of this project.

## CHAPTER 5: RESULTS WITH THE MATHEMATICAL MODEL

In Chapter 5, the proposed control scheme will be designed for the mathematical model obtained in Chapter 2. Several simulation scenarios will be conducted to demonstrate the effectiveness of the control scheme in regulating the position of the trolley, and cable length, and showcasing the remarkable vibration suppression capabilities of the proposed method.

### 5.1 Implementation of the control scheme for mathematical model

#### 5.1.1 Designing the ADRCs

From the equation of motion (2.8), the differential equations for the trolley displacement  $x(t)$  and the cable length  $l(t)$  can be expressed as follows, simplifying the form of Equation (3.1):

$$\begin{aligned}\ddot{x}(t) &= f_x(t, \dot{x}, x, \dot{l}, l, \dot{\theta}, \theta, F_l) + \frac{m_p + m_h}{m_t m_p + m_t m_h + m_p m_h} F_x \\ &= f_x(t, \dot{x}, x, \dot{l}, l, \dot{\theta}, \theta, F_l) + b_{0x} F_x\end{aligned}\quad (5.1)$$

$$\begin{aligned}\ddot{l}(t) &= f_l(t, \dot{x}, x, \dot{l}, l, \dot{\theta}, \theta, F_x) + \frac{m_p + m_t}{m_t m_p + m_t m_h + m_p m_h} F_l \\ &= f_l(t, \dot{x}, x, \dot{l}, l, \dot{\theta}, \theta, F_x) + b_{0l} F_l\end{aligned}\quad (5.2)$$

To achieve simultaneous positioning of the trolley and cable length, we will select a settling time of  $T_{settle} = 3$  seconds and an observer gain of  $k_{ESO} = 10$  for both the trolley position and cable length ADRC controllers. Based on Section 3.2 and the system parameters provided in Table 2.1, we can compute the parameters of the two ADRCs in Table 5.1. The payload mass is chosen as  $m_p = 1$  kg, within the range of  $[0.5, 1.5]$  kg, in order to evaluate the robustness of the ADRC in response to payload mass variations.

*Table 5.1 Parameters of ADRCs*

Parameter	Trolley position controller, ADRC1	Cable length controller, ADRC2
$b_0$	0.21052	0.26315
$s_{CL}$	-1.95	-1.95
$K_P$	3.8025	3.8025
$K_D$	3.9	3.9
$s_{ESO}$	-19.5	-19.5
$l_1$	58.5	58.5
$l_2$	1140.75	1140.75
$l_3$	7414.875	7414.875

The simulations of ADRC in MATLAB/Simulink are depicted in Figure 5.1.

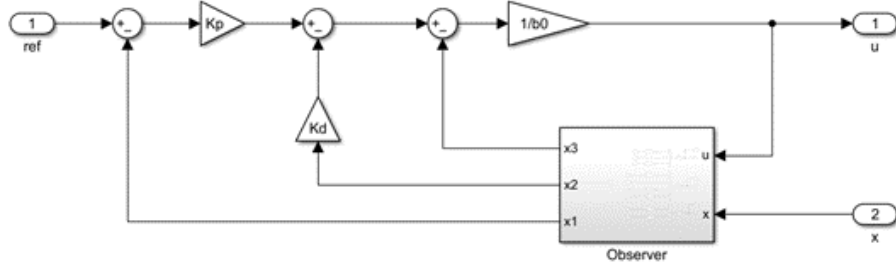


*Figure 5.1 The simulation of ADRC controller*

### 5.1.2 Designing the RBFN-IS

The PSO algorithm will be implemented in MATLAB. To maintain a fixed cable length, the initial cable length value will be set to be the desired value for the ADRC2 controller. The initial and target positions for the trolley will be set to 0 and 1 m, respectively. The PSO algorithm will then be utilized to search for the optimal parameters of the Input Shaping technique for each cable length and payload mass combination, aiming to minimize the fitness function (4.18). The parameters of PSO algorithm are chosen as Table 5.2.

*Table 5.2 The parameters of PSO algorithm*

Parameter	Value
$w$	0.4-0.9
$c_1$	2
$c_2$	2
Number of particles	10
Maximum number of iterations	40
$\eta_1$	1
$\eta_2$	1

With a cable length ranging from 0.2 m to 0.7 m and a payload mass ranging from 0.5 kg to 1.5 kg, the optimal parameters of the Input Shaping technique are summarized in Table 5.3.

*Table 5.3 Optimal Input Shaping parameters*

Sample no.	Payload mass, $m_p$ (kg)	Cable length, $l$ (m)	$t_2$	$t_3$
1	0.5 kg	0.2	0.4479	0.8969
2		0.25	0.5017	1.0030
3		0.3	0.5490	1.0983
4		0.35	0.5934	1.1868
5		0.4	0.6340	1.2684
6		0.45	0.6728	1.3458
7		0.5	0.7097	1.4186
8		0.55	0.7434	1.4879
9		0.6	0.7764	1.5537
10		0.65	0.8091	1.6168
11		0.7	0.8389	1.6780
12	1 kg	0.2	0.4487	0.8975
13		0.25	0.5006	1.0027
14		0.3	0.5499	1.0990
15		0.35	0.5929	1.1864
16		0.4	0.6345	1.2691
17		0.45	0.6731	1.3452
18		0.5	0.7092	1.4184
19		0.55	0.7420	1.4872
20		0.6	0.7770	1.5542
21		0.65	0.8095	1.6167
22		0.7	0.83864	1.6785
23	1.5 kg	0.2	0.4466	0.8973
24		0.25	0.5011	1.0034
25		0.3	0.5489	1.0982
26		0.35	0.5931	1.1866
27		0.4	0.6335	1.2684
28		0.45	0.6732	1.3459
29		0.5	0.7090	1.4183
30		0.55	0.7430	1.4880
31		0.6	0.7746	1.5534
32		0.65	0.8074	1.6170
33		0.7	0.8393	1.6767

The labeled dataset, consisting of five-sixths of the results obtained in Table 5.3, was utilized to train the RBF networks, while the remaining data was kept for

testing to assess the mapping capability of the two networks. The training process employed the gradient descent method with a learning rate  $\eta = 0.1$  and momentum factor  $\alpha = 0.05$ . The initial center points were randomly selected from the input data in Table 5.3, and all the hidden nodes had an initial width of 1, while the weights were initialized to 0.1. The performance index of the training procedure, defined by Equation 4.8, is depicted in Figure 5.2. It shows the progress of the training process in each epoch. Utilizing the training code in MATLAB, the parameters of the RBF networks are obtained as follows.

- RBF Network for  $t_2$  approximation:

$$\mathbf{c} = \begin{bmatrix} 0.78484 & 0.38340 & 0.94198 & 1.04288 & 1.00704 \end{bmatrix}^T$$

$$\mathbf{b} = \begin{bmatrix} 0.56198 & 0.92247 & 0.91069 & 0.83283 & 0.71518 \end{bmatrix}^T$$

$$\mathbf{w} = \begin{bmatrix} 0.62166 & -0.18703 & 0.18785 & 0.31206 & 0.53220 \end{bmatrix}^T$$

- RBF Network for  $t_3$  approximation:

$$\mathbf{c} = \begin{bmatrix} 0.86210 & 0.95117 & 1.23251 & 1.07160 & 0.71567 \end{bmatrix}^T$$

$$\mathbf{b} = \begin{bmatrix} 0.59279 & 0.73336 & 0.72161 & 0.71934 & 0.49828 \end{bmatrix}^T$$

$$\mathbf{w} = \begin{bmatrix} 0.77414 & 0.41435 & 0.55647 & 0.58562 & 0.72954 \end{bmatrix}^T$$

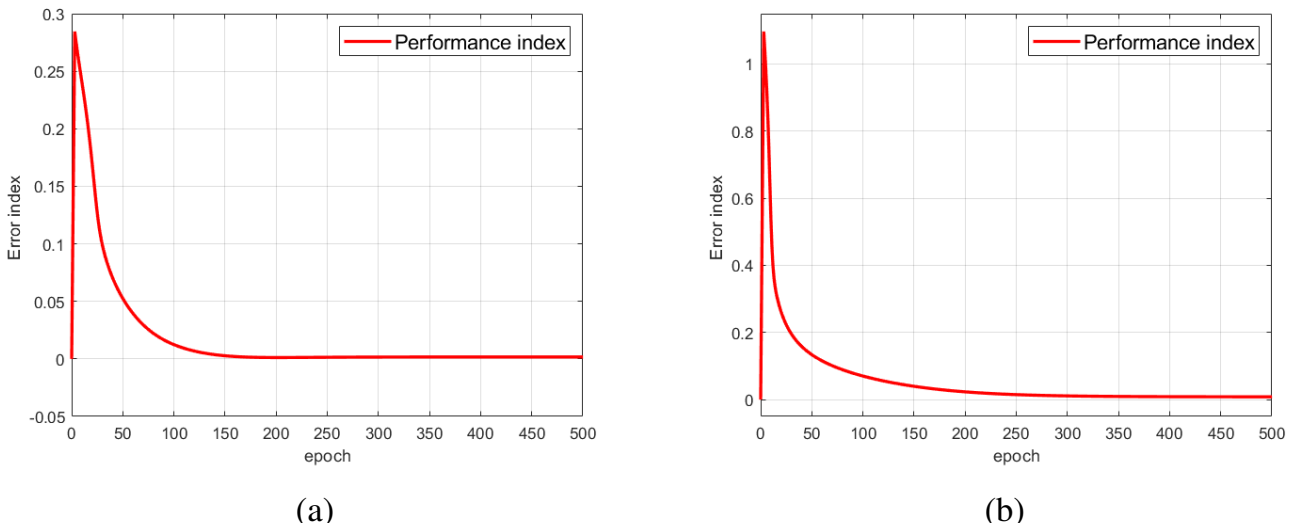


Figure 5.2 The performance index during training process for (a)  $t_2$  and (b)  $t_3$

To assess the approximation ability of the obtained RBF networks, we will utilize the relative error as a performance index, defined as:

$$\delta = \frac{|y - \hat{y}|}{y} \times 100\% \quad (5.3)$$

where  $y$  and  $\hat{y}$  represent the actual value and the approximate value obtained from the RBF network, respectively. The relative error for five randomly chosen samples is summarized in Table 5.4.

*Table 5.4 Approximation errors*

Sample no.	5	14	17	21	29
$t_2$	0.6340	0.5499	0.6731	0.8095	0.7090
$\hat{t}_2$	0.6291	0.5475	0.6712	0.8115	0.7035
$\delta$	0.7729	0.4364	0.2823	0.2471	0.7757
$t_3$	1.2684	1.0990	1.3452	1.6167	1.4183
$\hat{t}_3$	1.2588	1.0895	1.3398	1.6221	1.4218
$\delta$	0.7569	0.8644	0.4014	0.3340	0.2468

From the table, we can observe that the maximum relative error  $\delta$  for  $t_2$  and  $t_3$  are relatively small, being 0.7757 % and 0.8644 % respectively. This demonstrates that the obtained RBF networks are capable of providing optimal parameters for Input Shaping based on the measured cable length and payload mass as input.

## 5.2 Simulation results

To assess the effectiveness of the proposed strategy, a comparison will be made with the ADRC controller combined with a ZVD shaper designed based on two average frequency methods [10]. Since the exact values cannot be determined, the damping ratio for the computed parameters of these two shapers will be set to 0. The natural frequency of a single pendulum will be calculated using the formula  $\omega = \sqrt{g/l}$ . The first method involves designing the ZVD based on the average frequency, which is the average value of the frequencies corresponding to the maximum and minimum cable lengths, yielding the Average Operating Frequency-ZVD (AOF-ZVD). The frequency corresponding to a cable length of 0.2 m is determined to be 7.0035 rad/s, while for a cable length of 0.7 m, the frequency is found to be 3.7435 rad/s. Taking the average of these two frequencies, we obtain an average frequency of 5.3735 rad/s. The second scheme is the Average Operating Length ZVD (AOL-ZVD), where the natural frequency is calculated based on a cable length of 0.45 m, which is the average of the minimum length of 0.2 m and the maximum length of 0.7 m in the hoisting process. As from Equation 4.2, the parameter values for the AOF-ZVD and AOL-ZVD are presented in Table 5.5.

*Table 5.5 Parameters of AOF-ZVD and AOL-ZVD*

Average Operating Frequency ZVD					
$A_1$	$A_2$	$A_3$	$t_1$	$t_2$	$t_3$
0.25	0.5	0.25	0	0.5846	1.1692
Average Operating Length ZVD					
$A_1$	$A_2$	$A_3$	$t_1$	$t_2$	$t_3$
0.25	0.5	0.25	0	0.6728	1.3457

There will be two simulation cases considered based on the payload's movement:

Case 1: Lifting the payload

Case 2: Lowering the payload

In Case 1, the cable length will be adjusted with the objective of reducing it from an initial value of 0.7 m to 0.2 m. Moving on to Case 2, the payload will undergo a controlled descent from its initial position, characterized by a cable length of 0.2 m, to a new position with a cable length of 0.7 m. In all two cases, the trolley's initial position at 0 m will be adjusted to reach a desired setpoint of 1 m. Moreover, the two ADRC controllers will be set to simultaneously control the trolley and payload to reach their desired positions in 3 seconds. The objective is to achieve a zero payload swing, and the performance index will be chosen similarly to the fitness function of PSO, including the maximum amplitude (MA) and the Integral Absolute Error (IAE) of swing angle error. Once again, a lower index value indicates better swing suppression. Additionally, the payload mass of 0.75 kg are used. It's worth noting that this value are not included in the labeled dataset, allowing us to verify the approximate performance of the RBFN-IS. The simulation of the overall control structure in MATLAB/Simulink is depicted in Figure 5.3.

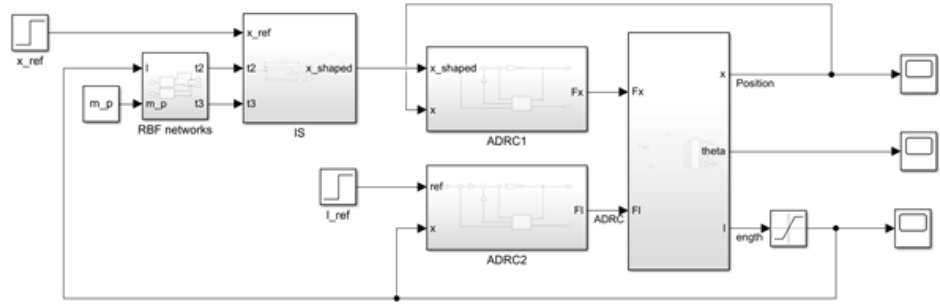


Figure 5.3 The simulation of overall control structure

### 5.2.1 Lifting the payload

Considering Case 1, we have obtained the following results.

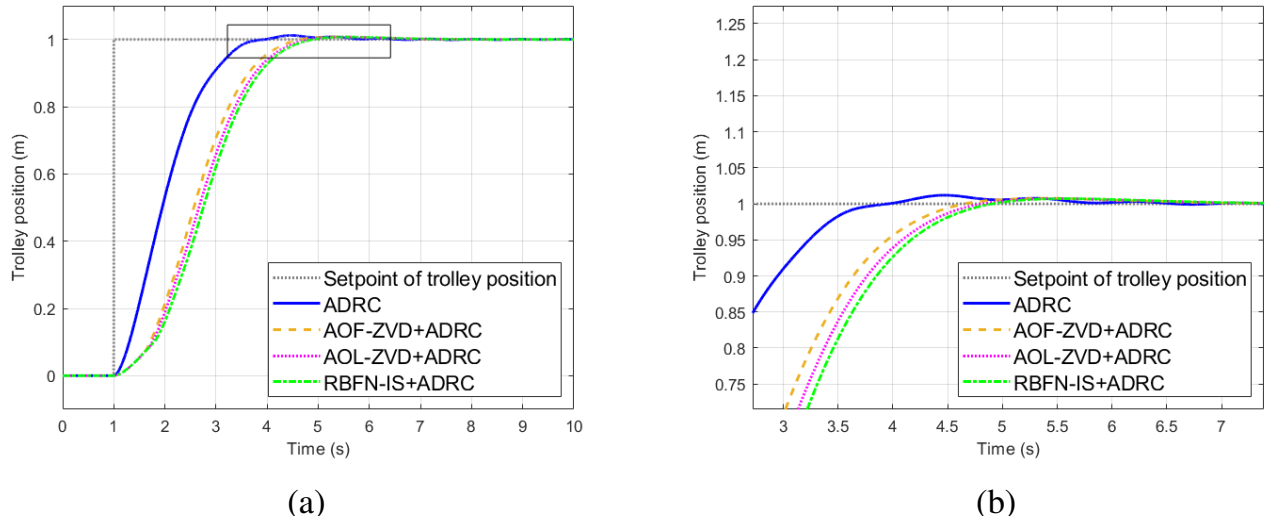
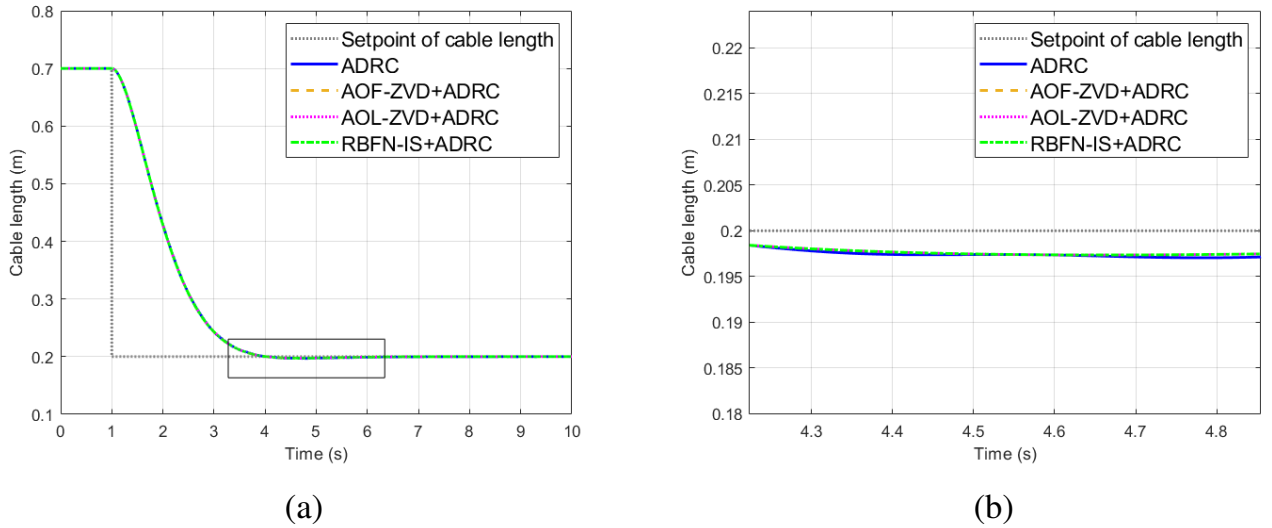


Figure 5.4 Trolley position response in Case 1

Table 5.6 Trolley position response in Case 1

Control Scheme	Trolley Position Response	
	Overshoot (%)	Settle time (seconds)
ADRC	1.1936	2.471
AOF-ZVD+ADRC	0.77155	3.263
AOL-ZVD+ADRC	0.74166	3.398
RBFN-IS+ADRC	0.71418	3.486

From Figure 5.4 (a), it is evident that all four control schemes, including ADRC, ADRC with AOF-ZVD, ADRC with AOL-ZVD, and ADRC with RBFN-IS, effectively controlled the trolley's position, closely tracking the desired values. The settle times were close to the desired  $T_{settle} = 3$  seconds, and the overshoots were relatively small (less than 1.2%) (Table 5.6). Furthermore, Figure 5.4 (b) demonstrates the ADRC's efficient disturbance rejection capability, particularly in the case with the largest payload oscillation angle. The incorporation of Input Shaping slightly delays the crane's position response. Among the Input Shaping cases, the RBFN-IS method exhibits the slowest settle time (3.486 seconds). Nevertheless, it still performs comparably to the traditional methods, AOF-ZVD, and AOL-ZVD, with settle times of 3.263 seconds and 3.398 seconds, respectively.



*Figure 5.5 Cable length response in Case 1*

*Table 5.7 Cable length response in Case 1*

Control Scheme	Cable Length Response	
	Overshoot (%)	Settle time (seconds)
ADRC	1.4803	2.784
AOF-ZVD+ADRC	1.3296	2.776
AOL-ZVD+ADRC	1.3274	2.776
RBFN-IS+ADRC	1.3258	2.776

Regarding the cable length response in Figure 5.5 (a), the settle times are relatively similar in all cases, approximately 2.776 seconds, satisfying the desired  $T_{settle} = 3$  seconds. The overshoots in these cases are relatively small (less than 1.5%), with the largest overshoot in scheme ADRC being 1.4803%. Similar to the position response,

all control schemes demonstrate effective disturbance rejection capability caused by payload oscillations (Figure 5.5 (b)).

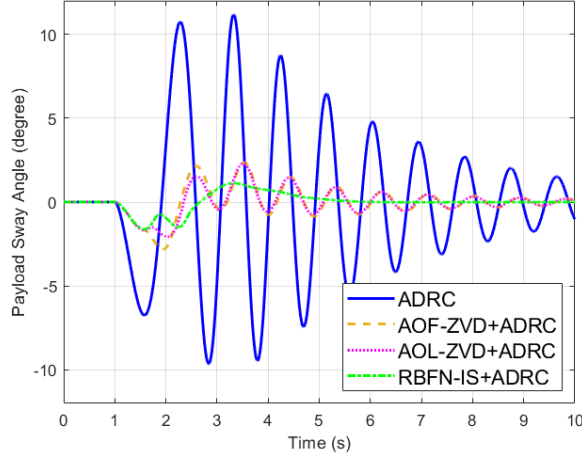
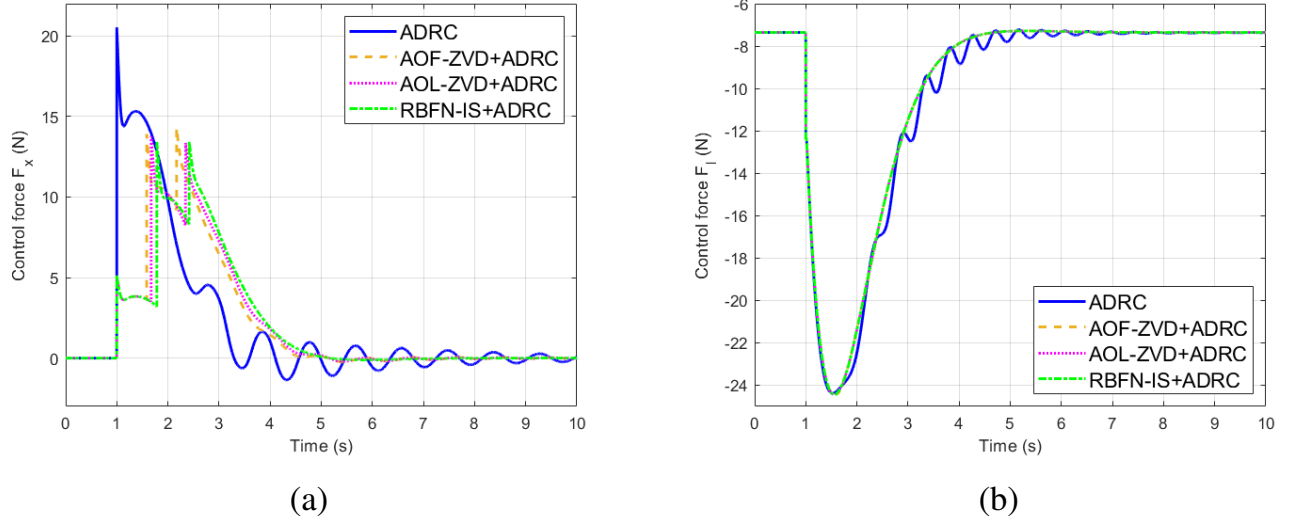


Figure 5.6 Payload sway angle in Case 1

Table 5.8 Payload sway angle in Case 1

Control Scheme	Payload Sway Angle	
	IAE (degree.seconds)	MA (degrees)
ADRC	32.8557	11.2745
AOF-ZVD+ADRC	6.2004	2.8122
AOL-ZVD+ADRC	5.4403	2.306
RBFN-IS+ADRC	3.1865	1.6111

In Figure 5.6, it is evident that in cases where only ADRC is utilized without Input Shaping, the payload exhibits the strongest oscillations. The IAE and MA values are 32.8557 degree.seconds and 11.2745 degrees, respectively (Table 5.8). By incorporating Input Shaping, the ability to suppress oscillations is significantly improved. Among the utilizing Input Shaping cases, AOF-ZVD shows the least effective oscillation suppression, reducing IAE and MA by 81.12% and 75.05% compared to the case without Input Shaping, respectively. Although the utilization of AOF-ZVD and AOL-ZVD has improved the oscillation suppression, some residual oscillation of about 0.3 degrees remains. In comparison, the RBFN-IS approach shows remarkable improvements by eliminating residual oscillations. Moreover, the RBFN-IS control scheme achieves the most significant reductions in IAE and MA value by 90.30% and 85.71%, respectively.



*Figure 5.7 (a) Control force for trolley position in Case 1, (b) Control force for cable length in Case 1*

In Figure 5.7 (a), it can be observed that the incorporation of Input Shaping results in a decrease in the maximum value of  $F_x$  from 20.533 N to approximately 14 N. Additionally, when not using Input Shaping, the control effort increases due to the larger impact of disturbances caused by payload oscillations. From Figure 5.7 (b), at the initial state,  $F_l$  will have a value of  $-m_p g = -7.3575$  N. In the scheme with only ADRC, the control effort remains the highest due to the influence of payload oscillations. In the remainings schemes,  $F_l$  shows relatively similar behavior.

### 5.2.2 Lowering the payload

Considering Case 2, we have obtained the following results.

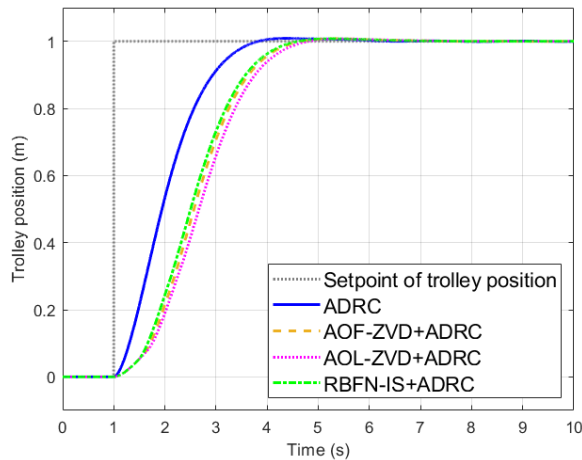


*Figure 5.8 Trolley position response in Case 2*

*Table 5.9 Trolley position response in Case 2*

Control Scheme	Trolley Position Response	
	Overshoot (%)	Settle time (seconds)
ADRC	0.87274	2.506
AOF-ZVD+ADRC	0.79798	3.265
AOL-ZVD+ADRC	0.74219	3.404
RBFN-IS+ADRC	0.76681	3.192

In Figure 5.8, all control schemes effectively regulate the trolley's position with a relatively small overshoot. The highest overshoot, around 0.87274%, and the fastest settling time of 2.506 seconds are yielded by ADRC scheme. Additionally, Figure 5.8 shows that the RBFN-IS+ADRC scheme provides improved performance, specifically, it achieves the shortest settle time of 3.192 seconds in comparison with AOF-ZVD and AOL-ZVD, which have settle times of 3.265 seconds and 3.404 seconds, respectively.

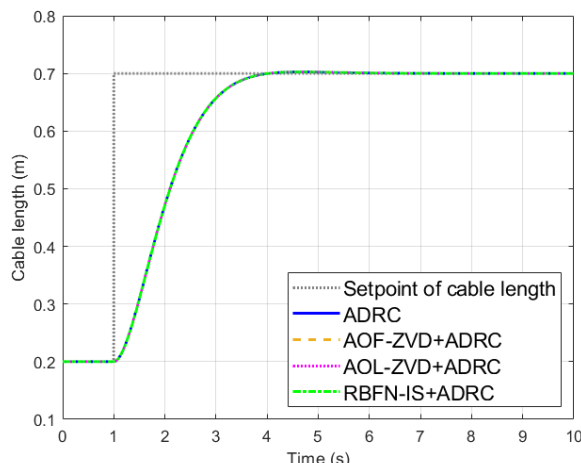


*Figure 5.9 Cable length response in Case 2*

*Table 5.10 Cable length response in Case 2*

Control Scheme	Cable Length Response	
	Overshoot (%)	Settle time (seconds)
ADRC	0.84150	2.371
AOF-ZVD+ADRC	0.84519	2.369
AOL-ZVD+ADRC	0.84502	2.369
RBFN-IS+ADRC	0.84621	2.369

Regarding cable length (Figure 5.9), all control schemes continue to show effectiveness in tracking the setpoint within the desired settle time. Furthermore, the overshoot in all the schemes is relatively small, just about 0.84% (Table 5.10).

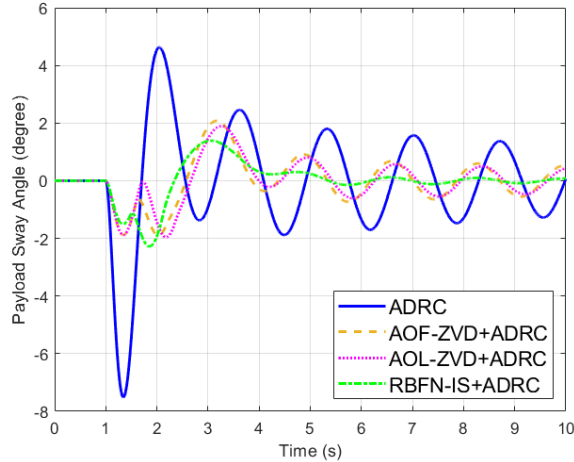


*Figure 5.10 Payload sway angle in Case 2*

*Table 5.11 Payload sway angle in Case 2*

Control Scheme	Payload Sway Angle	
	IAE (degree.seconds)	MA (degrees)
ADRC	13.3555	7.5638
AOF-ZVD+ADRC	5.9921	2.0625
AOL-ZVD+ADRC	5.3931	1.9888
RBFN-IS+ADRC	3.9416	2.301

Figure 5.10 demonstrates the effectiveness of Input Shaping in reducing sway oscillations. In the case using only ADRC, the payload's sway angle has an IAE value of 13.3555 degree.seconds and an MA value of 7.5638 degrees (Table 5.11). By using RBFN-IS, sway oscillations are significantly reduced, resulting in the best performance with a 70.48% and 69.57% reduction in IAE and MA, respectively, furthermore, the residual oscillation is nearly eliminated. AOF-ZVD and AOL-ZVD also show some improvement in sway suppression, but to a lower extent compared to RBFN-IS, reducing IAE by 55.13% and 59.61% respectively. The residual oscillations in these cases are around 0.5 degrees.

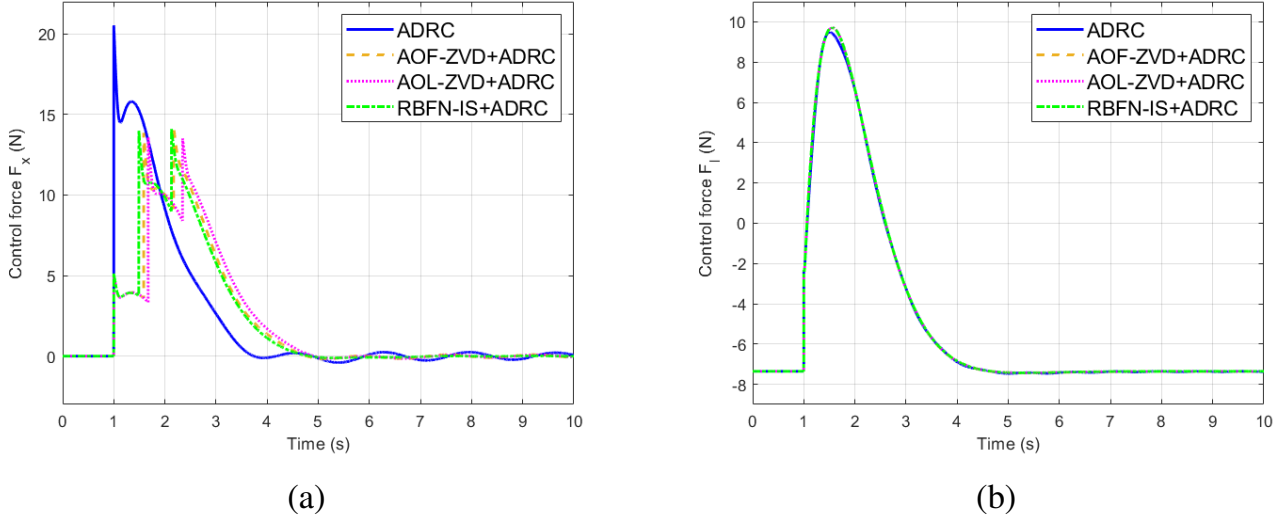


*Figure 5.11 (a) Control force for trolley position in Case 2, (b) Control force for cable length in Case 2*

In Figure 5.11, it is evident that the Input Shaping control schemes reduce the control effort of the driving force  $F_x$ , with the highest value being around 14.249 N in comparison with value of 20.5335 N in the scheme only using ADRC. The sway oscillations of the payload are smaller in these cases, resulting in smaller control efforts for  $F_x$  and  $F_l$  to counteract the effects of internal disturbances caused by residual oscillations. The driving force  $F_l$  remains relatively consistent among the different control schemes (Figure 5.11 (b)).

### 5.3 Chapter's Conclusion

In Chapter 5, the control scheme for the mathematical model of the overhead crane system was designed based on the theoretical foundations discussed earlier. The simulation results demonstrate the precise control of the trolley's position, accurate regulation of the cable length, and effective suppression of internal disturbances caused by the payload oscillations through the implementation of the two Active Disturbance Rejection Controls. Additionally, the utilization of Radial Basis Function networks to update the parameters of the Input Shaping method has improved the vibration suppression capabilities of the system when faced with changes in the model parameters.

## CHAPTER 6: RESULTS WITH THE EXPERIMENTAL MODEL

Chapter 6 will present the experimental overhead crane model. Subsequently, the control scheme for this model will be designed and experiments will be conducted to test the effectiveness of the proposed control scheme.

### 6.1 Experimental crane model

The experimental overhead crane model consists of two main components (Figure 6.1):

- The hardware system, which includes the crane structure and the electrical cabinet.
- The control system, comprising the user interface, programming software, laptop control, and the NI-myRIO 1900 Kit.

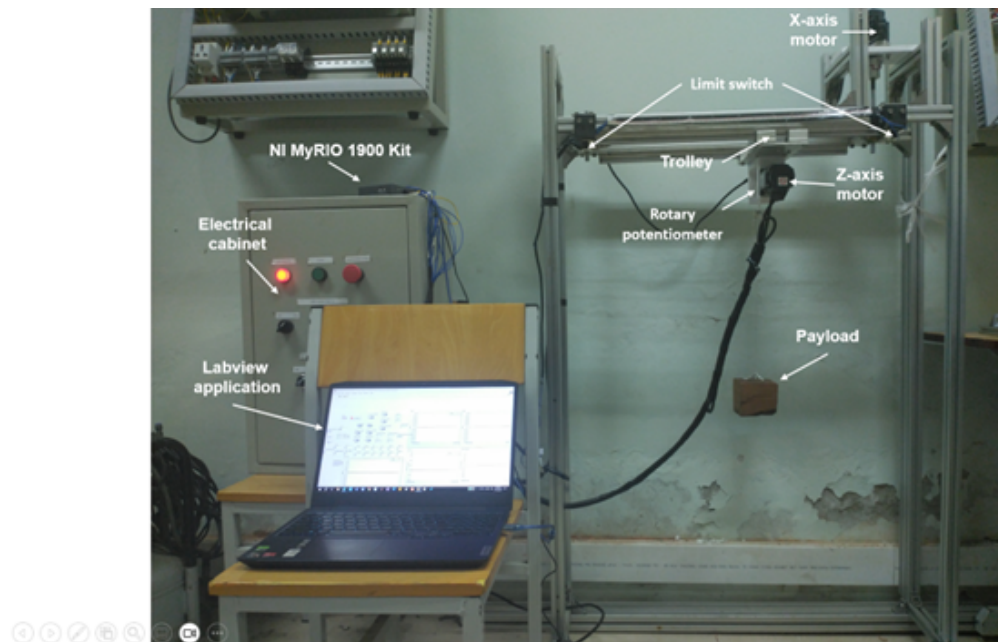


Figure 6.1 The experimental crane model

#### 6.1.1 Hardware system

The experimental overhead crane comprises a frame and beams, a trolley, a  $X$ -axis motor, a  $Z$ -axis motor, rotary potentiometer, limit switches, and a payload. The crane model is designed for movement along two axes,  $X$  and  $Z$ , achieved by controlling two motors. The trolley moves along the  $X$ -axis, while the hoist handles the  $Z$ -axis motion. When the trolley reaches the travel limit and triggers the limit switches, the model is automatically disconnected to ensure safety. The two motors

used to control the X and Z axes of the overhead crane are Mitsubishi HG-KN23J-S100 servo motors, equipped with the following basic specifications:

- Small motor size with an output power of 200W
- Maximum rotational speed: 3000 revolutions per minute (rpm)
- No electromagnetic brake
- Encoder with a resolution of 131072 pulses per revolution

The load of the system is designed as a single pendulum. It consists of a mass attached to the hook, forming a simple pendulum that swings freely during the crane's movement. The oscillation angle of the load will be determined using a rotary potentiometer, which will provide continuous measurements of the payload's angular displacement.

### **6.1.2 Electrical cabinet**

The external control panel of the electrical cabinet includes power indicator lights, start buttons, and emergency stop buttons, along with motor control switches, providing operators with a safe and user-friendly way to power on and control the motion of the overhead crane's axes.

Inside the electrical cabinet, there are two motor drivers responsible for controlling the two axes of the crane, along with power relays and safety devices to ensure safe operation during control. These motor drivers, manufactured by Mitsubishi with the model MR-JE-20A, receive control signals from the control system, process them, and drive the motors accordingly. Additionally, these drivers read encoder signals from the motors and feed them back to the control system to determine the precise position. The specifications of the Mitsubishi MR-JE-20A servo driver include:

- Power Supply: 200-240VAC
- Input Current: 1.5A
- Output Current: 1.5A
- Frequency: 50/60Hz
- Power Rating: 200W

The use of these reliable and high-performance motor drivers ensures smooth and precise control of the crane's movements, contributing to its overall safety and efficiency during operation.

### **6.1.3 NI myRIO 1900 Kit**

NI-myRIO is an integrated hardware and software controller, manufactured by National Instruments (NI) (Figure 6.2). It serves as an independent embedded platform that allows users to design and build real-time systems faster than ever before. This controller combines a dual-core ARM processor and an embedded FPGA chip on a System on a Chip (SoC) architecture. Additionally, NI-myRIO is equipped with various built-in input/output (I/O) capabilities, integrated WiFi, and a robust housing. Commonly used in education, research, and practical applications, NI-myRIO 1900 serves in control systems, testing and measurements, and automation tasks.



*Figure 6.2 The NI-myRIO 1900*

The hardware components of the NI-myRIO 1900 Kit consist of the following main parts (Figure 6.3):

- NI-myRIO 1900
- myRIO Expansion Port (MXP) for extension
- Power supply cable
- USB connection cable
- USB Host cable
- LED indicators
- Mini System Port (MSP)
- Input/output audio port cable
- Push-button

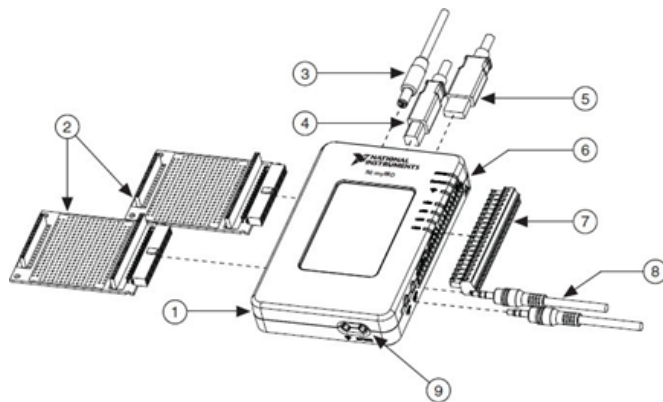


*Figure 6.3 The hardware components of the NI-myRIO 1900 Kit*

NI-myRIO includes 2 MSP ports and 1 MXP port. The MXP port supports two connector types, A and B. The I/O functions and pinouts on both connectors are identical, and the software specifies which I/Os are used on each connector. The I/O pins on the MSP and MXP ports are illustrated in Figures 6.4 and 6.5, respectively. Table 6.1 and 6.2 will provide a more detailed description of each pin on these two type of ports.

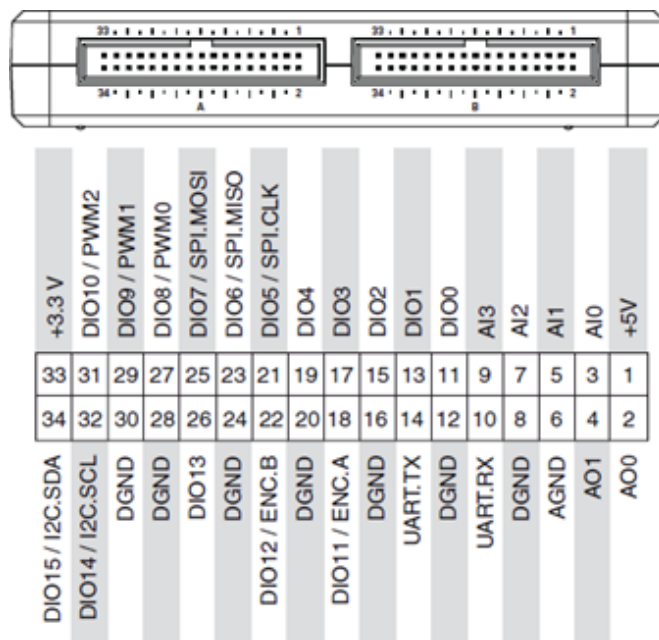


*Figure 6.4 The I/O pins on the MSP ports*

*Table 6.1 The pin description of the MSP ports*

Pin	Signal Type	Description
+5V	Ouput	5V power supply to external devices
AI<0...1>	Input	Analog Input Channel <0...1>
AGND	N/A	Analog Input Ground
+3.3V	Ouput	3.3V power supply to external devices
DIO<0...15>	Input or Output	Digital I/O Channel <0...15>
UART.RX	Input	UART Receive Pin
UART.TX	Ouput	UART Transmit Pin
DGND	N/A	Digital Input Ground

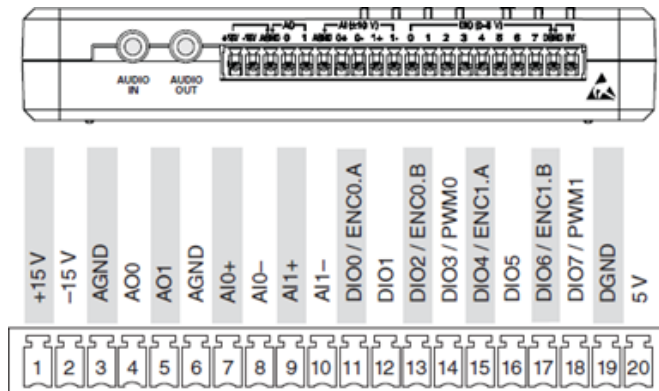


*Figure 6.5 The I/O pins on the MXP port*

*Table 6.2 The pin description of the MXP port*

Pin	Signal Type	Description
+15V/-15V	Output	+15V/-15V power supply to external devices
AI0+/AI0-	Input	Analog Input Channel 0
AI1+/AI1-	Input	Analog Input Channel 1
AO<0...1>	Output	Analog Input Channel <0...1>
+5V	Output	5V power supply to external devices
DIO<0...7>	Input or Output	Digital I/O Channel <0...7>
DGND	N/A	Digital Input Ground

#### 6.1.4 Labview application

LabVIEW (Laboratory Virtual Instrument Engineering Workbench) is a specialized graphical programming software developed by National Instruments. It comes bundled with National Instruments' devices, including NI-myRIO. With LabVIEW, users can quickly and efficiently create control, measurement, testing, and automa-

tion programs for various systems and devices. Additionally, LabVIEW can also be used as a monitoring and operation interface. The programming approach in LabVIEW is fundamentally different from traditional programming languages like C or Pascal. Instead of using conventional symbols and syntax, users express their programs through visual representations in the editor, known as Graphical Programming (G). Key functionalities of LabVIEW include:

- Acquiring data from external devices such as temperature sensors, webcam images, motor speeds, and more.
- Processing various data types, such as analog signals, digital signals, images, audio, etc.
- Simulating and processing acquired data for research or specific system requirements.
- Communicating with peripheral devices through various communication standards like RS232, RS485, USB, PCI, Ethernet.

LabVIEW provides a user-friendly and intuitive environment for programming, making it accessible to both beginners and experienced engineers for a wide range of applications in the fields of control, automation, data acquisition, and analysis.

## **6.2 Implementation of the control scheme for experimental model**

### ***6.2.1 Designing the ADRCs***

To design the ADRCs controller, we first need to perform the identification of the transfer functions of the two X and Z axis motors. The LabVIEW program provides the control voltage to the two drivers, as shown in Figure 6.6. The analog output ports AO0 and AO1 limit the control voltage within the range of [-10,10]. Both drivers are set to the speed control mode, where the motor speed is proportional to the control voltage with a rate of 30 rpm/V. The speed of the trolley and the rate of change of the cable length for different control voltages are depicted in Figures 6.7 and 6.8.

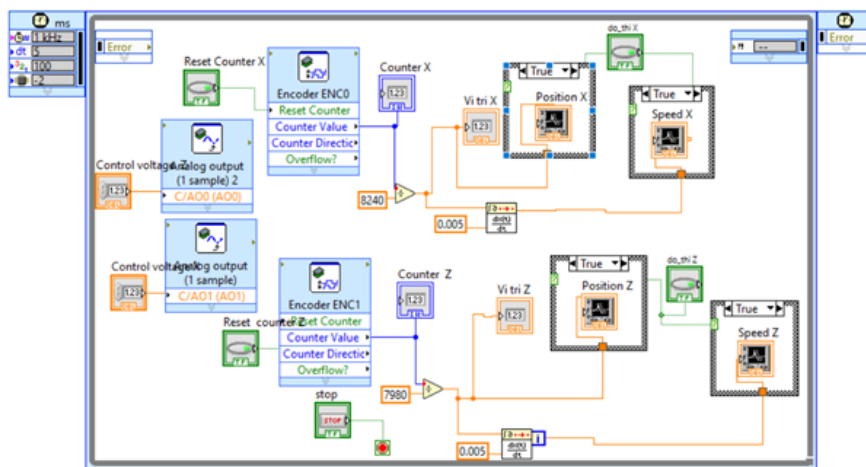


Figure 6.6 The LabVIEW program for motors identification

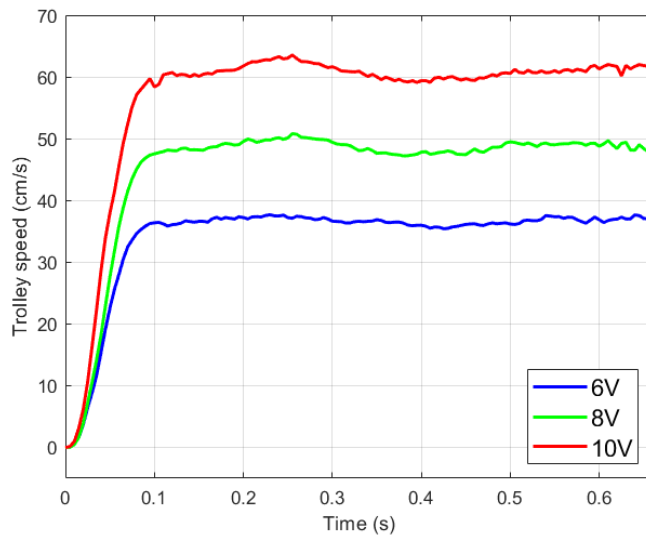


Figure 6.7 Trolley speed for different control voltages

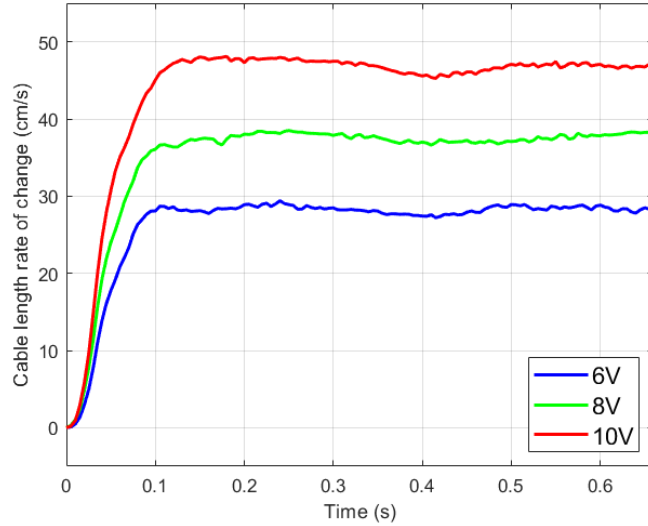


Figure 6.8 Rate of change of cable length for different control voltages

Using the "systemIdentification" toolbox in MATLAB, we obtained the first-order transfer functions for the trolley's speed and the rate of change of the cable length in the form of:

$$G_{Vx} = \frac{V_x(s)}{U_x(s)} = \frac{6.1732}{0.040898s + 1} \quad (6.1)$$

$$G_{Vl} = \frac{V_l(s)}{U_l(s)} = \frac{4.7556}{0.040651s + 1} \quad (6.2)$$

From these transfer functions, the transfer functions between the trolley's position and the control voltage, and the cable length and the control voltage are obtained as follows:

$$G_x = \frac{X(s)}{U_x(s)} = \frac{1}{s} \frac{V_x(s)}{U_x(s)} = \frac{6.1732}{s(0.040898s + 1)} \quad (6.3)$$

$$G_l = \frac{L(s)}{U_l(s)} = \frac{1}{s} \frac{V_l(s)}{U_l(s)} = \frac{4.7556}{s(0.040651s + 1)} \quad (6.4)$$

Taking the inverse Laplace transform of the above equations, we obtain the second-order differential equations for the trolley's position and the cable length, respectively:

$$\begin{aligned} \ddot{x}(t) &= -\frac{1}{0.040898} \dot{x}(t) + \frac{6.1732}{0.040898} u_x(t) \\ &= f_x(t) + b_{0x} u_x(t) \end{aligned} \quad (6.5)$$

$$\begin{aligned} \ddot{l}(t) &= -\frac{1}{0.040651} \dot{l}(t) + \frac{4.7556}{0.040651} u_l(t) \\ &= f_l(t) + b_{0l} u_l(t) \end{aligned} \quad (6.6)$$

For practical implementation, we will set the settle time  $T_{settle} = 3$  seconds and the observer gain  $k_{ESO} = 100$  for both ADRCs. According to [2], the parameters of the observer for discrete ADRC can be computed with the sample time of  $T_{sample}$  as follows:

$$l_1 = 1 - (z_{ESO})^2 \quad (6.7)$$

$$l_2 = \frac{3}{2T_{sample}}(1 - z_{ESO})^2(1 + z_{ESO}) \quad (6.8)$$

$$l_3 = \frac{1}{T_{sample}^2}(1 - z_{ESO})^3 \quad (6.9)$$

where  $z_{ESO} = e^{s_{ESO}T_{sample}}$ . The parameters of the two ADRCs with  $T_{sample} = 0.005$  seconds are tabulated in Table 6.3.

*Table 6.3 Parameters of ADRCs*

Parameter	Trolley position controller, ADRC1	Cable length controller, ADRC2
$b_0$	150.941	116.986
$s_{CL}$	-1.95	-1.95
$K_P$	3.8025	3.8025
$K_D$	3.9	3.9
$s_{ESO}$	-195	-195
$l_1$	0.8577	0.8577
$l_2$	160.2595	160.2595
$l_3$	9663.2	9663.2

Two ADRC controllers in the LabVIEW program are illustrated in Figure 6.9.

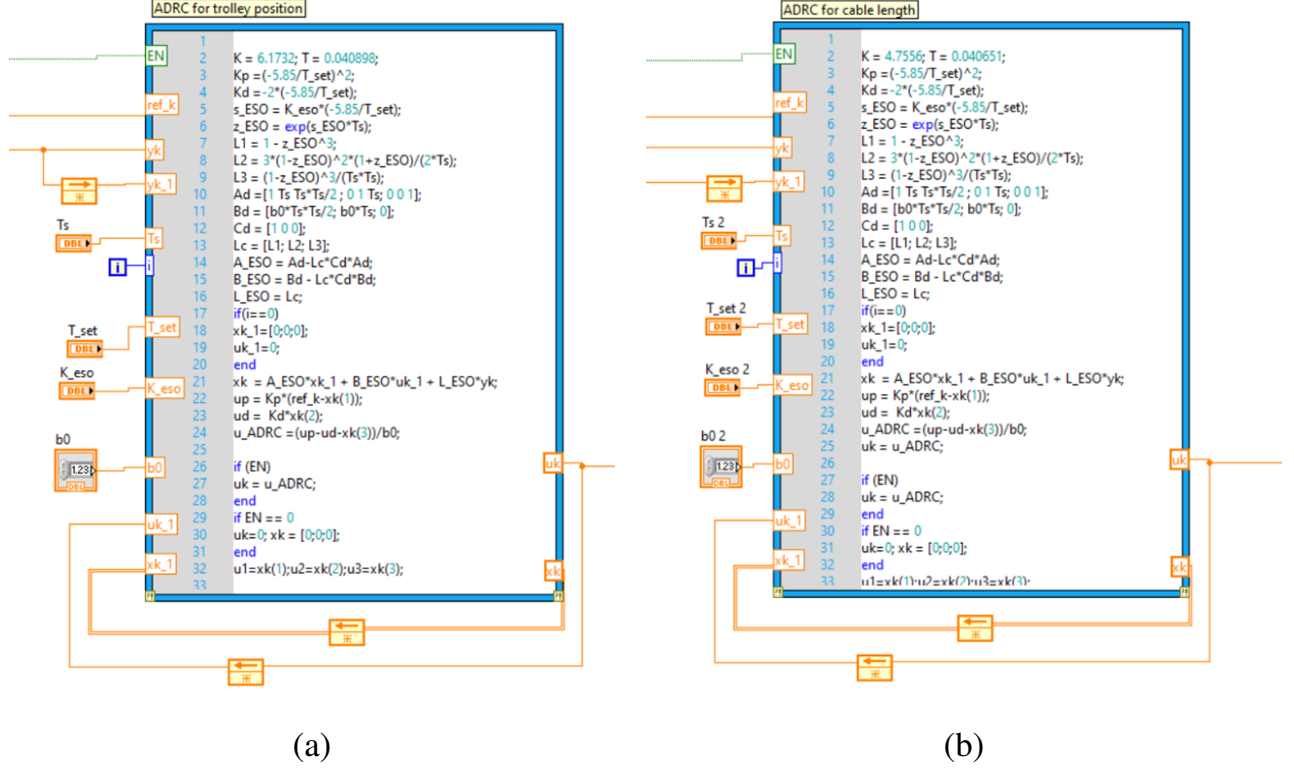


Figure 6.9 (a) ADRC controller for payload position, (b) ADRC controller for cable length

### 6.2.2 Designing the RBFN-IS

Firstly, we will utilize the PSO algorithm to search for the labeled dataset. According to [11], to apply PSO in this case, we will measure the payload oscillation angle with each fixed cable length. Subsequently, this oscillation angle will be used to find the corresponding optimal parameters  $t_2$  and  $t_3$  for that cable length using PSO. This method comprises two parts as shown in Figure 6.10.

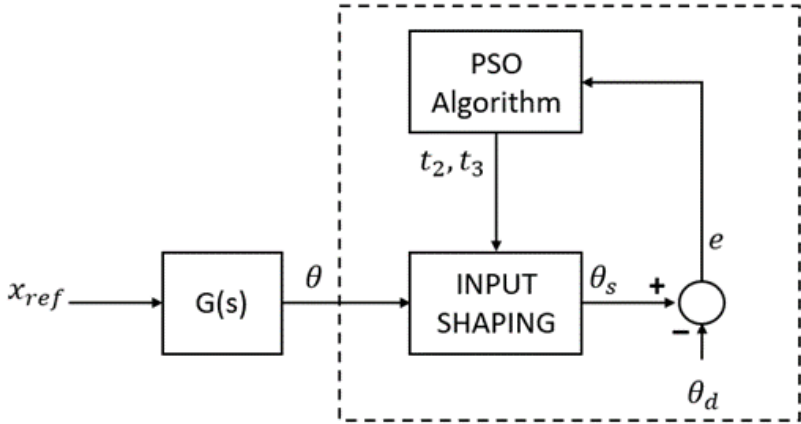


Figure 6.10 Input Shaping parameters selection using the PSO algorithm

The steps of this method are as follows:

- Step 1:  $G(s)$  represents the closed-loop system consisting of two ADRCs and the crane model with the input being the position setpoint  $x_{ref}$ , and the fixed cable length  $l$  and payload mass  $m_p$  as parameters. The output signal is the payload sway angle  $\theta$ , which will be recorded.
- Step 2:  $\theta$  will be fed into the transfer function of Input Shaping, and we obtain the suppressed sway angle  $\theta_s$ . Since Input Shaping is a feed-forward technique, changing its position behind the closed-loop system still allows us to test the vibration suppression capability of its parameters.
- Step 3:  $\theta_s$  is then subtracted by the desired sway angle  $\theta_d = 0$  degree to obtain the sway angle error  $e$ .
- Step 4: The signal  $e$  from Step 3 will be used to calculate the fitness function  $J(t)$ , as represented in (4.18), thereby updating the position and velocity of the particles according to the PSO algorithm.
- Step 5: Repeat steps 2-4 to find the optimal parameters  $t_2$  and  $t_3$  of the Input Shaping that yields the best vibration suppression capability for specific cable length  $l$  and payload mass  $m_p$ .

We will implement this method for cable lengths in the range of [0.2, 0.7] m and payload masses of 0.6, 0.8, and 1.3 kg. The parameters for the PSO algorithm will be selected in a manner similar to that described in Section 5.1.2. The optimal parameters obtained will be tabulated in Table 6.4.

*Table 6.4 Optimal Input Shaping parameters*

Sample no.	Payload mass, $m_p$ (kg)	Cable length, $l$ (m)	$t_2$	$t_3$
1	0.6 kg	0.2	0.4507	0.8958
2		0.25	0.5031	1.0073
3		0.3	0.5485	1.0997
4		0.35	0.5980	1.1854
5		0.4	0.6359	1.2668
6		0.45	0.6759	1.3436
7		0.5	0.7071	1.4225
8		0.55	0.7437	1.4847
9		0.6	0.7717	1.5505
10		0.65	0.8066	1.6219
11		0.7	0.8419	1.6800
12	0.8 kg	0.2	0.4519	0.8963
13		0.25	0.5025	1.0029
14		0.3	0.5525	1.0980
15		0.35	0.5969	1.1818
16		0.4	0.6386	1.2664
17		0.45	0.6681	1.3422
18		0.5	0.7089	1.4223
19		0.55	0.74058	1.4905
20		0.6	0.7736	1.5561
21		0.65	0.8060	1.6131
22		0.7	0.8426	1.6801
23	1.3 kg	0.2	0.4513	0.9019
24		0.25	0.5018	1.0072
25		0.3	0.5490	1.1025
26		0.35	0.5881	1.1830
27		0.4	0.6367	1.2676
28		0.45	0.6717	1.3467
29		0.5	0.7044	1.4173
30		0.55	0.7389	1.4895
31		0.6	0.7755	1.5495
32		0.65	0.8076	1.6166
33		0.7	0.8406	1.6743

Both the RBF networks will have the following structure: 2 input nodes, 5 hidden nodes, and 1 output node. Using the gradient descent algorithm, we obtain the

parameters of the networks as follows:

- RBF Network for  $t_2$  approximation:

$$\mathbf{c} = \begin{bmatrix} 0.59934 & 0.8500 & 0.9001 & 1.2766 & 0.7844 \end{bmatrix}^T$$

$$\mathbf{b} = \begin{bmatrix} 0.9557 & 0.8383 & 0.6048 & 0.7643 & 0.5321 \end{bmatrix}^T$$

$$\mathbf{w} = \begin{bmatrix} -0.1796 & -0.1300 & 0.4528 & 0.6474 & 0.6236 \end{bmatrix}^T$$

- RBF Network for  $t_3$  approximation:

$$\mathbf{c} = \begin{bmatrix} 0.86210 & 0.95117 & 1.23251 & 1.07160 & 0.71567 \end{bmatrix}^T$$

$$\mathbf{b} = \begin{bmatrix} 0.59279 & 0.73336 & 0.72161 & 0.71934 & 0.49828 \end{bmatrix}^T$$

$$\mathbf{w} = \begin{bmatrix} 0.0053 & 0.2248 & 0.8004 & 0.8653 & 1.1336 \end{bmatrix}^T$$

The RBFN-IS in LabVIEW program is depicted in Figure 6.11.

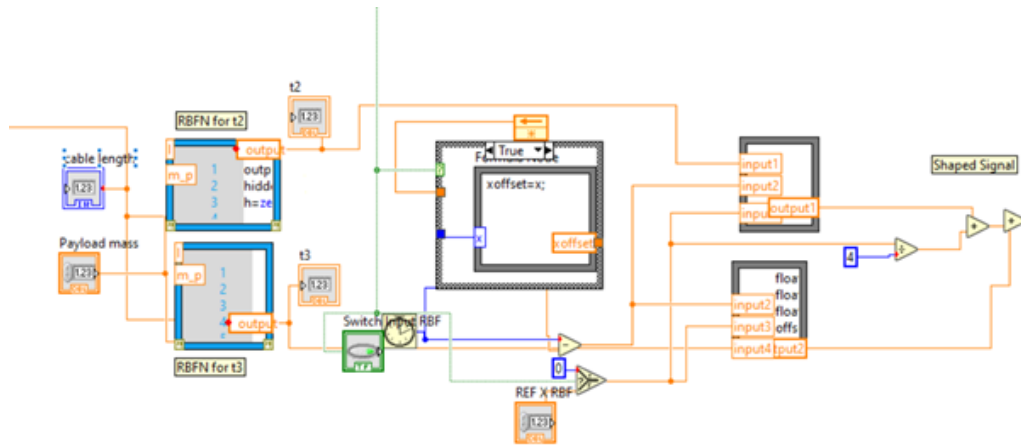


Figure 6.11 The Labview program for control

### 6.3 Experimental results

To evaluate the effectiveness of the proposed method, two scenarios similar to the simulation case will be used:

- Case 1: Lifting the payload
- Case 2: Lowering the payload

In these scenarios, the cable length will be varied from 0.2 m to 0.7 m, while the trolley will be controlled from position 0 to position 0.4 m. The payload mass will be chosen as 0.7 kg. Four control schemes similar to the simulation case will be used, where the parameters of AOF-ZVD and AOL-ZVD are listed in Table 6.5. The parameters of ADRCs and RBF networks used will be those obtained in Part 6.2.1 and 6.2.2.

*Table 6.5 Parameters of AOF-ZVD and AOL-ZVD*

Average Operating Frequency ZVD					
$A_1$	$A_2$	$A_3$	$t_1$	$t_2$	$t_3$
0.25	0.5	0.25	0	0.5846	1.1692
Average Operating Length ZVD					
$A_1$	$A_2$	$A_3$	$t_1$	$t_2$	$t_3$
0.25	0.5	0.25	0	0.6728	1.3457

### 6.3.1 Lifting the payload

In the case of lifting the payload from a position with a cable length of 0.7 m to 0.2 m, the following results are obtained.

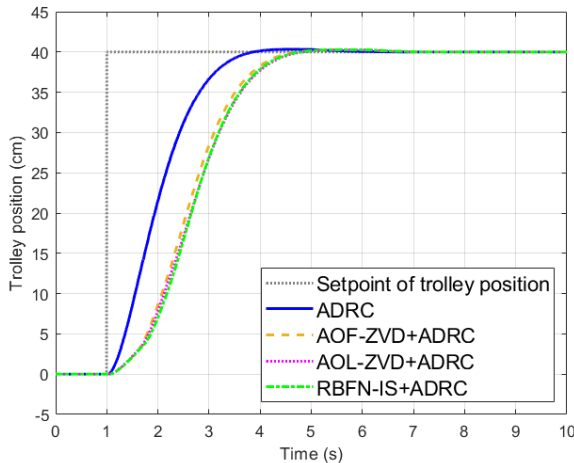


*Figure 6.12 Experimental trolley position response in Case 1*

*Table 6.6 Experimental trolley position response in Case 1*

Control Scheme	Trolley Position Response	
	Overshoot (%)	Settle time (seconds)
ADRC	0.8272	2.500
AOF-ZVD+ADRC	0.6415	3.265
AOL-ZVD+ADRC	0.5842	3.395
RBFN-IS+ADRC	0.7017	3.335

ADRC has demonstrated its ability to accurately control the trolley's position in all schemes with relatively small overshoots, with the highest value being 0.8272% in the ADRC scheme (Figure 6.12). The settling times in all schemes ensured the desired value of 3 seconds, with the shortest being 2.500 seconds in the ADRC scheme and the longest being 3.395 seconds in the AOL-ZVD+ADRC scheme (Table 6.6).

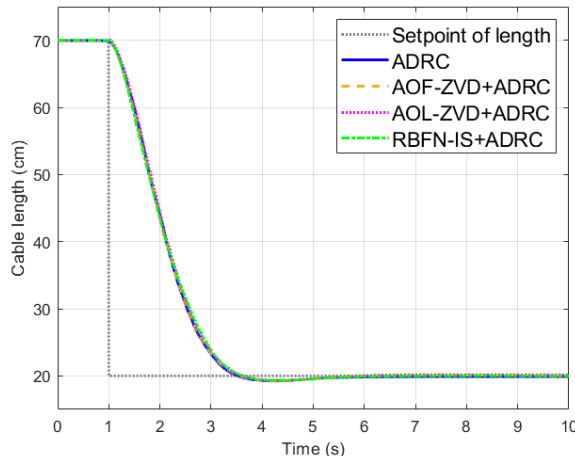


*Figure 6.13 Experimental cable length response in Case 1*

*Table 6.7 Experimental cable length response in Case 1*

Control Scheme	Cable Length Response	
	Overshoot (%)	Settle time (seconds)
ADRC	1.5161	2.475
AOF-ZVD+ADRC	1.5204	2.460
AOL-ZVD+ADRC	1.5123	2.520
RBFN-IS+ADRC	1.5129	2.505

From Figure 6.13 and Table 6.7, it can be observed that all the control schemes have demonstrated effective control of the cable length response, with relatively simi-

lar performance across the schemes. Although the overshoot values in all cases are approximately 1.5%, with the highest being 1.5204% for the AOF-ZVD+ADRC scheme, these values are still within acceptable limits. Additionally, the settle time is approximately 2.5 seconds, meeting the requirement of 3 seconds.

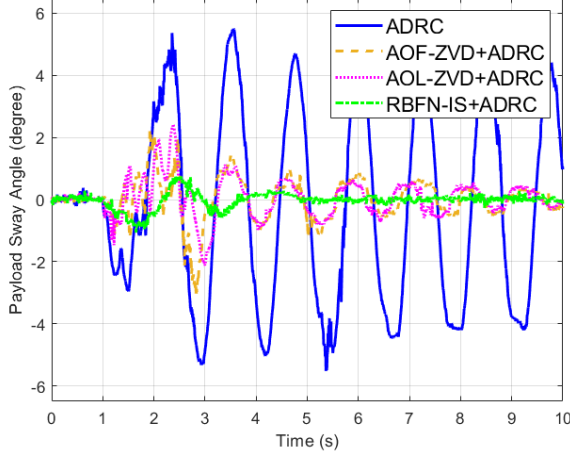


*Figure 6.14 Experimental payload sway angle in Case 1*

*Table 6.8 Experimental payload sway angle in Case 1*

Control Scheme	Payload Sway Angle	
	IAE (degree.seconds)	MA (degrees)
ADRC	26.9131	6.0020
AOF-ZVD+ADRC	4.9585	3.1507
AOL-ZVD+ADRC	4.6752	2.4182
RBFN-IS+ADRC	1.5734	1.0653

Figure 6.14 demonstrates that the incorporation of Input Shaping methods significantly reduces payload oscillations in practical scenarios. The various Input Shaping approaches allow for a minimum reduction of 81.57% and 47.51% in IAE and MA, respectively (Table 6.8), when using the AOF-ZVD scheme. Furthermore, the update of Input Shaping parameters through RBF network in the experiment shows substantial improvement in vibration suppression, with reductions of 94.15% in IAE and 82.25% in MA, which represents the best result among the utilized Input Shaping methods. Furthermore, the utilization of RBFN-IS has eliminated the residual oscillations of the payload.

From Figure 6.15, it can be observed that all control voltage signals are within the permissible range of  $[-10, 10]$  V. With the utilization of Input Shaping, the maximum control voltage is reduced from 4.4837 V in the case of using only ADRC to

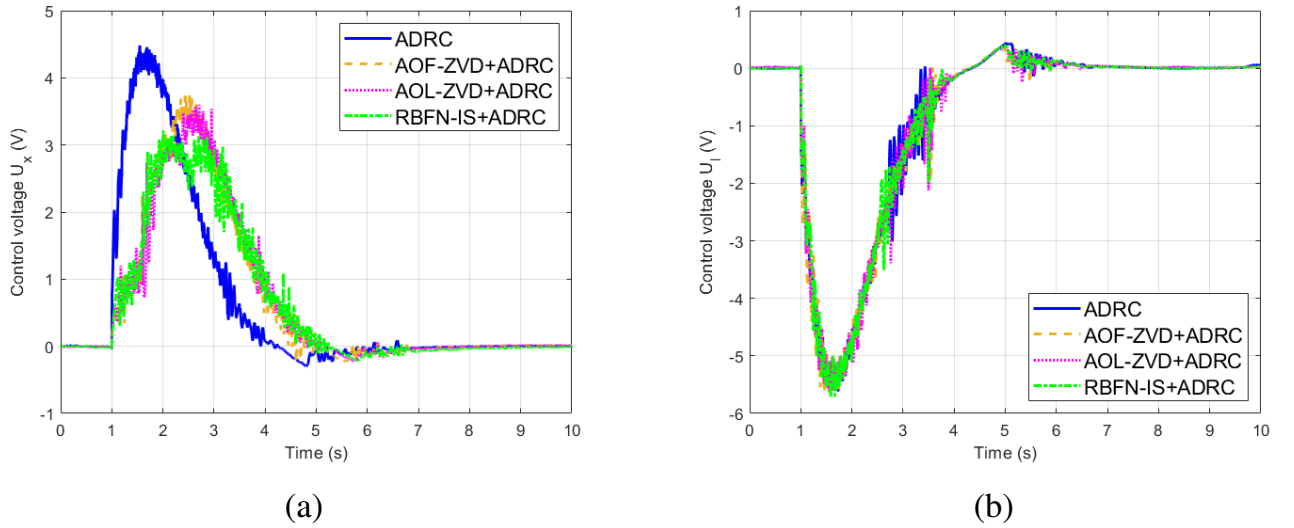


*Figure 6.15 (a) Control voltage for trolley position in Case 1, (b) Control voltage for cable length in Case 1*

approximately 3.2144 V in the case of combining RBFN-IS. For the control voltage signals responsible for cable length, the values are relatively similar across the schemes, with a maximum value of around 5.6 V.

### 6.3.2 Lowering the payload

In the case of lowering the payload from a position with a cable length of 0.2 m to 0.7 m, the following results are obtained.

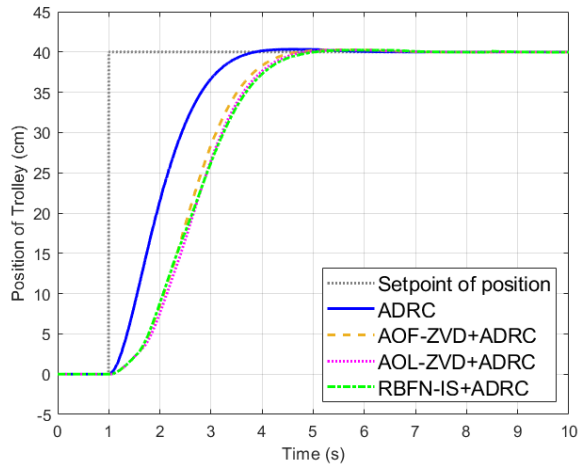


*Figure 6.16 Experimental trolley position response in Case 2*

*Table 6.9 Experimental trolley position response in Case 2*

Control Scheme	Trolley Position Response	
	Overshoot (%)	Settle time (seconds)
ADRC	0.8213	2.505
AOF-ZVD+ADRC	0.6467	3.260
AOL-ZVD+ADRC	0.5862	3.405
RBFN-IS+ADRC	0.5674	3.480

Similar to the payload lifting case, ADRC continues to demonstrate its effectiveness in all schemes, ensuring the trolley's position reaches the setpoint with settling times close to 3 seconds (Figure 6.16). Additionally, the overshoot in all schemes is relatively small, with the highest value being 0.8213% in the ADRC scheme (Table 6.9).

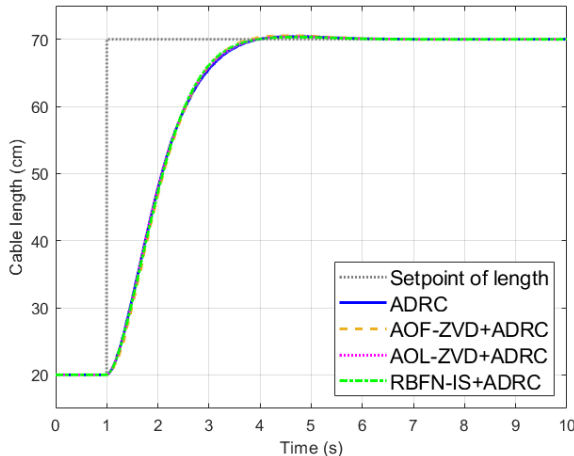


*Figure 6.17 Experimental cable length response in Case 2*

*Table 6.10 Experimental cable length response in Case 2*

Control Scheme	Cable Length Response	
	Overshoot (%)	Settle time (seconds)
ADRC	0.81724	2.4815
AOF-ZVD+ADRC	1.0579	2.3860
AOL-ZVD+ADRC	0.8552	2.3915
RBFN-IS+ADRC	0.8506	2.3985

From Figure 6.17 and Table 6.10, it can be observed that ADRC continues to demonstrate effective control of the cable length with an overshoot of only about

1%, which is smaller than the overshoot observed in the case of lifting the payload. Additionally, the settle time still meets the desired value of 3 seconds.

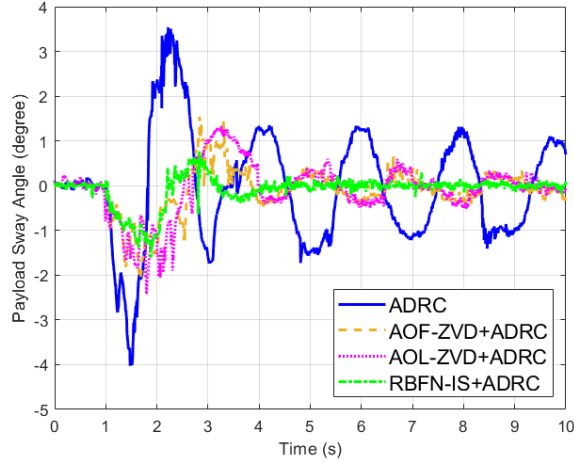


*Figure 6.18 Experimental payload sway angle in Case 2*

*Table 6.11 Experimental payload sway angle in Case 2*

Control Scheme	Payload Sway Angle	
	IAE (degree.seconds)	MA (degrees)
ADRC	9.9854	4.0284
AOF-ZVD+ADRC	3.3995	2.0818
AOL-ZVD+ADRC	4.1994	2.4272
RBFN-IS+ADRC	1.8244	1.6062

From Figure 6.18, it can be seen that the proposed scheme exhibits the best vibration suppression capability by eliminating the residual oscillations of the payload, with an MA value of only 1.6062 degrees. Furthermore, this method reduces the IAE value by 81.72%, while the AOF-ZVD and AOL-ZVD schemes reduce it by 65.95% and 57.94%, respectively. This clearly demonstrates the superior vibration suppression ability of RBFN-IS compared to traditional methods.

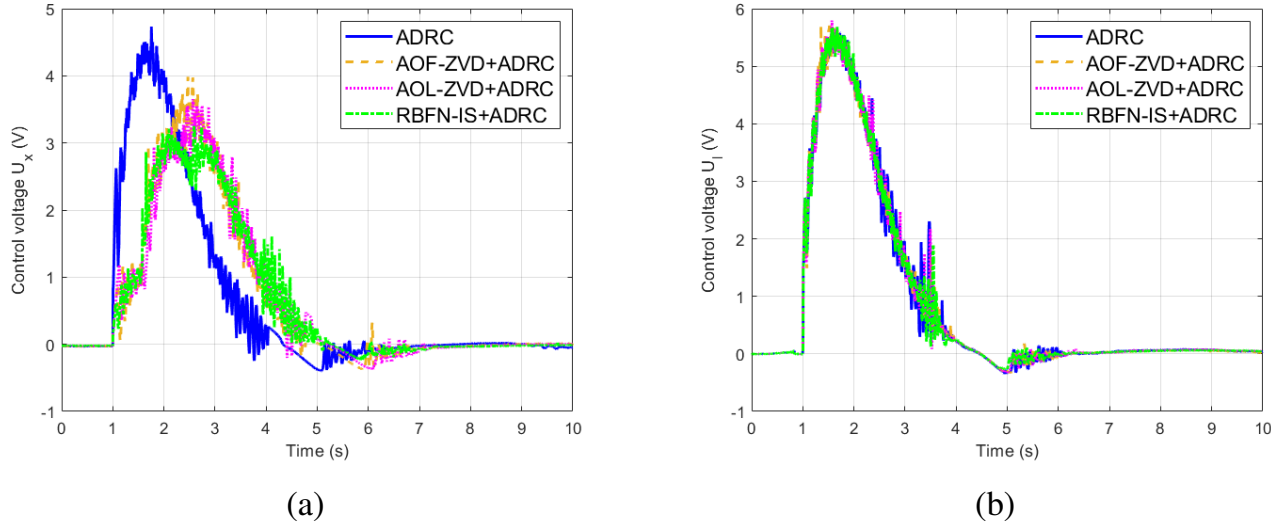


*Figure 6.19 (a) Control voltage for trolley position in Case 2, (b) Control voltage for cable length in Case 2*

Similarly to the case of lifting the payload, all control voltage signals are within the permissible range. The control voltage  $U_x$  is 4.7333 V in the case of using only ADRC (Figure 6.19 (a)). The control voltage for cable length remains relatively consistent across schemes, with the highest value being 5.7956 V in the AOL-ZVD+ADRC scheme (Figure 6.19 (b)).

#### 6.4 Chapter's Conclusion

Chapter 6 introduced the experimental overhead crane model and proceeded with the design of ADRCs by identifying the transfer functions of the two motors and designing RBFN-IS using the PSO algorithm. The results obtained from various scenarios have demonstrated the effective control and vibration suppression capabilities of the proposed method.

## CONCLUSION

After completing the project "Radial Basis Function based Input Shaping for Gantry Crane control," I am immensely grateful for the wholehearted support and assistance from my instructor, Dr. Đỗ Trọng Hiếu. With this dedicated support, I have made significant progress in fulfilling the project's objectives.

Throughout the project, I achieved the following results:

- Gained a profound understanding of the gantry crane system, including its practical aspects and the mathematical and experimental models associated with it.
- Acknowledged the theories of Active Disturbance Rejection Control, Input Shaping method, Radial Basis Function network, and Particle Swarm Optimization algorithm.
- Designed a control scheme combining ADRCs and RBFN-IS to regulate trolley position, cable length, and simultaneously reduce payload oscillations for both the mathematical and experimental models.
- Conducted effective verification of the proposed control scheme through simulations and experiments under various scenarios.

Future work will focus on improving the performance of ADRC by minimizing overshoot and reducing settling time. Additionally, the proposed approach will be validated on a 3-D gantry crane model with hoisting process.

## REFERENCES

- [1] J. Han, "From PID to Active Disturbance Rejection Control," in IEEE Transactions on Industrial Electronics, vol. 56, no. 3, pp. 900-906, March 2009, doi: 10.1109/TIE.2008.2011621.
- [2] G. Herbst, "A Simulative Study on Active Disturbance Rejection Control (ADRC) as a Control Tool for Practitioners," Electronics, vol. 2, no. 3, pp. 246–279, Aug. 2013.
- [3] Zhiqiang Gao, "Scaling and bandwidth-parameterization based controller tuning," Proceedings of the 2003 American Control Conference, 2003., Denver, CO, USA, 2003, pp. 4989-4996, doi: 10.1109/ACC.2003.1242516.
- [4] Neil C. Singer and Warren P. Seering. 1991. Preshaping command inputs to reduce system vibration. Artificial intelligence at MIT: expanding frontiers. MIT Press, Cambridge, MA, USA, 128–147.
- [5] C. -G. Kang, "Impulse Vectors for Input-Shaping Control: A Mathematical Tool to Design and Analyze Input Shapers," in IEEE Control Systems Magazine, vol. 39, no. 4, pp. 40-55, Aug. 2019, doi: 10.1109/MCS.2019.2913610.
- [6] Broomhead, D. & Lowe, D. (1988). Multivariable Functional Interpolation and Adaptive Networks. Complex Systems, 2, 321–355. doi:10.1007/s005210070033
- [7] Liu, Jinkun. (2013). Radial Basis Function (RBF) Neural Network Control for Mechanical Systems. 10.1007/978-3-642-34816-7\_11. doi:10.1109/acc.2013.6579874
- [8] Kennedy and R. Eberhart, "Particle swarm optimization," Proceedings of ICNN'95 - International Conference on Neural Networks, Perth, WA, Australia, 1995, pp. 1942-1948 vol.4, doi: 10.1109/ICNN.1995.488968.
- [9] Y. Shi and R. Eberhart, "A modified particle swarm optimizer," 1998 IEEE International Conference on Evolutionary Computation Proceedings. IEEE World Congress on Computational Intelligence (Cat. No.98TH8360), Anchorage, AK, USA, 1998, pp. 69-73, doi: 10.1109/ICEC.1998.699146.
- [10] Singhowe, W.E. & Porter, Lisa & Seering, W.P.. (1997). Input shaped control of a planar gantry crane with hoisting. 1. 97 - 100 vol.1. 10.1109/ACC.1997.611762.

- [11] Xu, Bo, Wang, Ran, Peng, Baoying, Alqurashi, Fahad Abdullah and Salama, Mohamad. "Automatic parameter selection ZVD shaping algorithm for crane vibration suppression based on particle swarm optimisation" Applied Mathematics and Nonlinear Sciences, vol.7, no.1, 3922, pp.73-82. <https://doi.org/10.2478/amns.2021.1.00075>

## APPENDIX

### Appendix 1. Research participation

- Participate in presenting a poster at "Hội nghị Sinh viên NCKH lần thứ 40 cấp Trường Điện - Điện tử năm học 2022-2023".



### Appendix 2

The experimental video can be accessed by scanning the QR Code below or through the following link: <https://www.youtube.com/watch?v=nXUntl9WLQQ>

